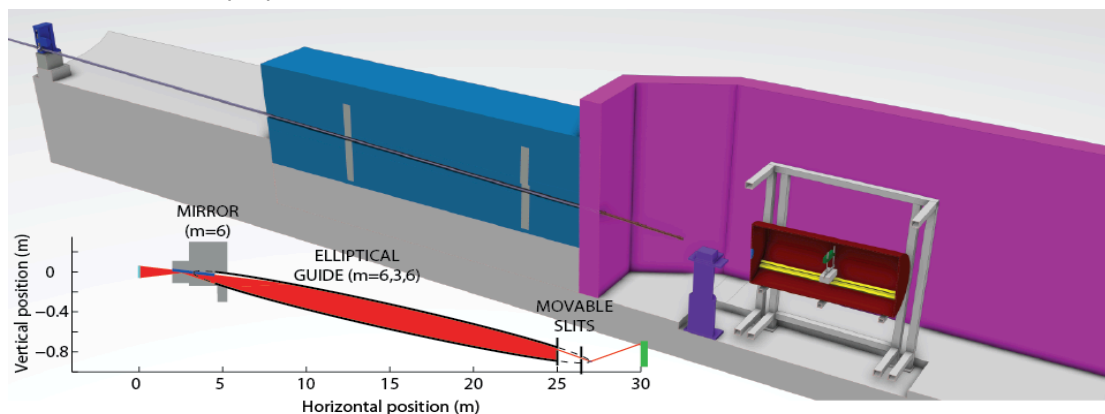




ESS Instrument Construction Proposal FREIA

Please read the call for instrument proposals found at europeanspallationsource.se/instruments2013 and the "Preparation and Review of an Instrument Construction Proposal" to guide you in preparing your instrument construction proposal.



	Name (name, title, e-mail address)	Affiliation (name of institution, address)
Proposer	Hanna Wacklin hanna.wacklin@esss.se	ESS
Co-proposers	Anette Vickery	NIB, Copenhagen University
ESS coordinator	Hanna Wacklin	

Note: All proposals received by ESS will be included as Expressions of Interest for In-kind contributions. ESS will use this information for planning purposes and the proposer or affiliated organization is not obligated to materially contribute to the project.

The following table is used to track the ESS internal distribution of the submitted proposal.

	Name
Document submitted to	Ken Andersen
Distribution	Dimitri Argyriou, Oliver Kirstein, Arno Hiess, Robert Connatser, Sindra Petersson Årsköld, Richard Hall-Wilton, Phillip Bentley, Iain Sutton, Thomas Gahl, relevant STAP

ENCLOSURES

<< FREIA_Appendix.pdf>>

EXECUTIVE SUMMARY [1-2 PAGES]

FREIA, the Fast Reflectometer for Extended Interfacial Analysis, is a versatile instrument optimised for high flux measurements of interfacial kinetics with a broad simultaneous Qz-range, allowing structural analysis of thin films (<100 Å) to be carried out at timescales relevant to colloidal and macro-molecular interactions at surfaces. The instrument has a horizontal sample geometry to allow these experiments at the widest possible range of interfaces, including free liquid surfaces, liquid-liquid, solid-liquid as well as solid-air interfaces. The instrument design has been optimised for the largest and fastest growing science areas of soft condensed matter and life sciences, where both the structure and formation of thin film samples as well as their response to environmental changes are of interest. Current scientific challenges that FREIA will address in particular include:

- self-assembly of surfactants, polymers and proteins at solid and liquid interfaces
- rearrangement processes in thin films (diffusion, annealing, exchange etc.)
- encapsulation and release in e.g. drug delivery materials, sensors and energy storage
- switchable materials that respond to external stimuli
- chemical and biochemical surface reactions

FREIA has an elliptical guide design focusing a neutron beam with a broad vertical divergence and wavelength range onto the sample surface, which allows measurements to be carried out without moving the sample. This is ideal for studying kinetics, as the angle of incidence can be changed between pulses using a fast shutter system to record the full Q-range effectively simultaneously.

FREIA can operate in a low-medium resolution mode using the full ESS pulse, and also incorporates a sophisticated chopper system for Wavelength Frame Multiplication (WFM) to provide experiments with a constant 2% wavelength resolution appropriate for thicker films up to 500Å, thus expanding the scientific scope to cover the vast majority of experiments in soft condensed matter, advanced materials and life science. FREIA exploits the advantages of the ESS long pulse source to the full, giving rise to significant improvements in measurement times. The kinetic mode using fast shutters will enable new science in all areas of thin film growth, self-assembly, rearrangement and surface reactions due to the extended simultaneous Q-range. The instrument design was optimised for 4cm x 4cm samples, but samples between 5mm x 5mm and 4cm x 10cm can be used efficiently.

FREIA will cater for most of the reflectometry science case apart from high resolution and polarised studies, and will ideally be complemented by a polarised reflectometer optimised for small samples and high-resolution, and a dedicated grazing-incidence SANS/off-specular instrument for determining lateral structures.

MXType.Localized
Document Number MXName
Project Name <<project name>>
Date 01/11/2013

TABLE OF CONTENTS

ENCLOSURES	2
Executive Summary [1-2 Pages]	2
Table of Contents	3
1. Instrument Proposal [app. 20 pages]	4
1.1 Scientific Case [5 pages]	4
1.2 Description of Instrument Concept and Performance [10 pages].....	8
1.3 Technical Maturity [3 pages]	25
1.4 Costing [2 pages].....	26
2. List of Abbreviations	28

MXType.Localized
Document Number MXName
Project Name <<project name>>
Date 01/11/2013

1. INSTRUMENT PROPOSAL

1.1 Scientific Case

Neutron reflectometry at ESS

Neutron reflectometry covers a very broad spectrum of science involving the growth, self-assembly, structure and interactions of a wide variety of thin films and has an impact on all the core areas of the ESS materials science case. Considering that the advanced thin film materials of the future will be increasingly complex, there is an urgent and continued need to develop high performance neutron reflectometers to elucidate their structure. The strong European user base and facilities mean that there is also a need to be ambitious and differentiate the ESS reflectometry suite from existing instruments.

Reflectometry is very well suited to the ESS long pulse time structure, with significant gains expected due to the high cold neutron flux and the relatively relaxed resolution requirements, which allow the full pulse width to be used for many experiments. The time averaged flux of the ESS is estimated to be comparable to the ILL cold source, which gives rise to a peak ESS flux of approximately 25 times higher given the 14Hz frequency and 2.86ms pulse length at 5MW. For reflectometry, the ESS offers a possibility to relax the experimental resolution up to the source resolution to gain more usable flux, up to the equivalent of the time-averaged ILL cold source flux on the sample. In contrast, time-of-flight instruments at reactor sources need to employ pulse shaping choppers, which typically only transmit ~1-2% of the source intensity to the sample. However, the wide range of film thicknesses of interest place a broad range of requirements on instrument resolution and in many cases require the use of pulse shaping choppers at ESS, in which case the expected performance is proportional to the resolution. Given that there are overall a broad range of requirements on sample size, resolution and bandwidth in reflectometry experiments, it is crucial to optimise a suite of instruments with specific capabilities to enable all of the areas of the science at a world leading level.

The user community

Figure 1 shows the distribution of scientific papers published in the last 10 years for the largest scientific areas that use reflectometry, according to records kept by the facilities (ISIS, ILL, HZB, SNS, NIST, ANSTO and PSI are included). It should be noted that the graph does not include all papers found, and that many papers involve more than once of the keywords used. The largest sections of the user community today are interested in in soft condensed matter, polymers and life science, which have a significant overlap with more general chemistry and materials science at surfaces. Comparing the evolution of publications between 2003-2007 (339) with those in 2008-2013 (507), the total number of unique publications has risen by 50%, reflecting that a number of new instruments have come available within this period (for example FIGARO, Inter, Polref, Offspec, MARIA, Platypus). In addition to this, particular growth has occurred in the areas of life science, kinetics, polarised neutron reflectometry (PNR) and liquids. In this context "kinetics" represents all papers involving kinetics, diffusion, rearrangement, reactions or interactions at surfaces, which have or could have used time-resolved reflectometry. "Liquids" represents all science on free liquid surfaces, i.e. air-solution, air-water and liquid-liquid interfaces.

MXType.Localized
Document Number MXName
Project Name <<project name>>
Date 01/11/2013

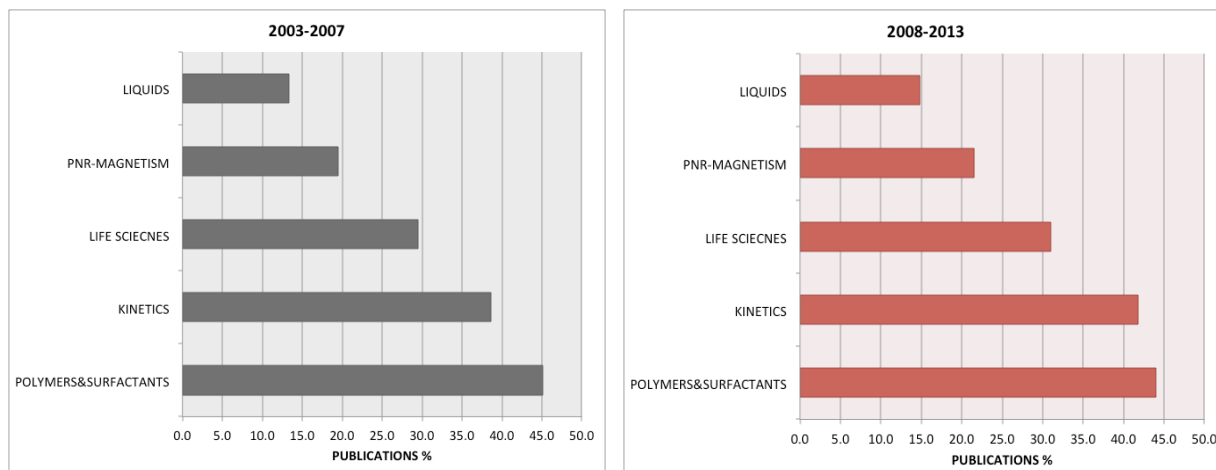


Figure 1. Reflectometry publications in the largest scientific areas during the last 5 and 10 years, based on publication records from ISIS, ILL, HZB, SNS, NIST and PSI. Note that not all the papers are included in this graph, and that many papers involve several of the keywords used.

The user community is vibrant, and it is common for one publication to cite several instruments and facilities. A typical oversubscription factor lies between of 2-3 for most instruments.

The Science case for FREIA - Kinetics

The proposed FREIA instrument has been optimised for the largest and fastest growing science areas of soft condensed matter and life sciences, where both the structure and formation as well as response to environmental changes of thin film samples are of interest. The optimisation of FREIA is however also highly suitable for a wide range of materials chemistry and hard condensed matter science as well, with the exception of very high-resolution and polarised experiments.

The challenges to be met in soft condensed matter and life sciences areas are as wide ranging as the topics investigated, but due to strong development of time-of-flight reflectometers in the past 10 years, there is a clear trend to follow time-dependent processes. These include, but are not limited to:

- Self-assembly of surfactants, polymers and proteins at solid and liquid interfaces
- Rearrangement processes in thin films: e.g. polymer interdiffusion, inter-layer movement (e.g. lipid flip-flop), annealing/drying/exchange/wetting processes in composite films such as photovoltaic materials.
- Encapsulation and release of components in e.g. plastics, polymer blends, drug delivery and implant materials, chemical and biological sensors
- Switchable materials that undergo structural changes in response to external stimuli (chemical, mechanical, electrical or electromagnetic) with potential device applications
- Surface reactions that involve change in the film structure or chemical composition; e.g. enzyme catalysis, oxidation or other film degradation reactions, receptor-ligand binding, drug-target interactions, surface functionalisation etc.

MXType.Localized
Document Number MXName
Project Name <<project name>>
Date 01/11/2013

The kinetics in these systems can be investigated in-situ by many surface sensitive techniques from neutron and X-ray reflection, ellipsometry/dual polarisation interferometry, quartz crystal microbalance to scanning probe and fluorescence microscopies. Most of these techniques however either lack chemical sensitivity to the sample composition, or require invasive labelling to derive this information.

Time-of-flight (tof) neutron reflectometry offers the possibility to record a range of Qz-values simultaneously, allowing determination of both structure and chemical composition as function of time. Deuterium labelling in soft condensed, organic or biological materials also gives the measurements a unique sensitivity to the composition of multicomponent samples, which is of great importance for both fundamental studies and technological applications. The usefulness of tof-reflectometry critically depends on the ability to match both the time-resolution and the dynamic Qz-range of the measurements to the structural changes investigated. The time and length scales that can potentially be followed by neutron reflectometry in such systems vary from a few to several hundred Ångströms, and from milliseconds to minutes, or even hours. Today, large samples (up to 30mm x 100mm) are used to reach time resolutions on the second-minute scale on world-leading reflectometers, such as FIGARO at ILL, or Inter at ISIS TS2. At ESS it should be possible to reach sub-second time resolution on samples that are of comparable size, or alternatively to use the flux gain to reduce the sample size by an order of magnitude. The main challenge is that these kinetic measurements are typically only possible within a limited Qz-range, as to record the full Q-range of interest would involve reconfiguring the instrument 1-2 times to access different angles of incidence.

The FREIA Solution

The key scientific driver for FREIA is to allow fast kinetic measurements on the ms-s timescale with the broadest possible simultaneous Qz-range. To make the best use of the ESS cold source flux, a novel guide and collimation system has been developed for this purpose, which allows the entire Qz range to be accessed without any movement of the instrument optics or the sample. The horizontal design with a variable resolution will cater for a broad range of interfaces and samples, making it a versatile instrument that will ideally be complemented by a polarised reflectometer optimised for smaller samples and high-resolution studies, and a dedicated grazing-incidence SANS/off-specular instrument for 2D-3D film structure. Below is a small selection of examples of the type of scientific challenges for which FREIA is optimised.

Scientific Challenges for FREIA:

- Fast adsorption and desorption processes: Figure 2a shows the fastest acquisition times for determining the surface excess in thin films to a reasonable accuracy on FIGARO, which are in the region of 30-40s. Applications that need faster acquisition times include atmospheric chemistry (oxidation of aerosol surfaces), and surfactant and polymer adsorption at both static and dynamic interfaces. At ESS it should be possible to monitor such processes in the sub-second to second time-region, which is inaccessible to neutrons today.

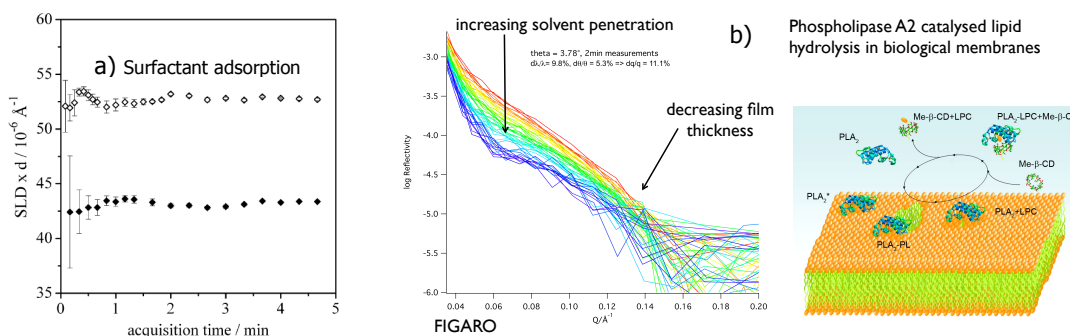


Figure 2. a) Minimum acquisition time to determine the scattering length density of a thin surfactant film (b) 2 min. measurements of enzyme catalyzed lipid hydrolysis in the broadest possible simultaneous Q-range. Both measured on FIGARO using the $d\lambda/\lambda=7.25\%$ FWHM. From Campbell, R. A., H. P. Wacklin, et al. (2011) EPJ Plus 126, 107.

- Biological interactions: The initial interactions of proteins and enzymes with cell membranes are of great interest for determining biological mechanisms underlying both health and disease. The challenge lies in observing a broad enough dynamic Q-range. For example in phospholipase A₂ catalyzed lipid hydrolysis, the enzyme causes both structural and compositional changes that occur over a wide range in Q. Figure 2b shows such data recorded in 1-2min in D₂O solutions in which the contrast is good and the reaction is slowed down 10 times due to isotope effects. On FREIA it will be possible to study the kinetics of this biochemical reaction in H₂O.
- Liquid-liquid interfaces (e.g. oil-water): These interfaces are difficult to study due to the drastic beam attenuation by the liquids, and as a consequence, μm-thick spin coated oil-films are used to mimic these systems (Zarbakhsh, et al. Meas Sci Technol, 1999,10, 738.) The ESS flux will offer a significant reduction in the experimental path length, which should allow real liquid-liquid interfaces to be investigated.
- In-situ studies of inter-diffusion at buried interfaces: Many studies today use multiple samples in which a process has been annealed or quenched at different times in order to study mechanisms that would ideally be studied in-situ. Applications include many technologically important materials such as photovoltaic materials, polymer multilayers, and energy materials. For example the early-stage kinetics of deuterium adsorption into hydrogen storage materials as shown in Figure 3 could be studied in-situ on FREIA.

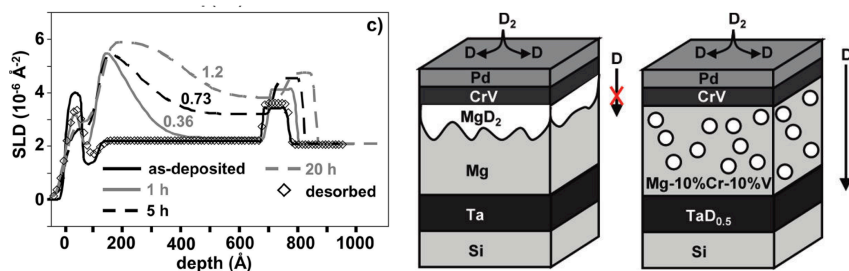


Figure 3. Deuterium adsorption into hydrogen storage materials monitored in annealed samples at different times. From Kalisvaart, W. P., E. J. Luber, et al. (2012). J. Phys. Chem. C **116**(9): 5868-5880.

MXType.Localized
Document Number MXName
Project Name <<project name>>
Date 01/11/2013

- Chemically or biologically active samples for industrial and medical applications, which need high-throughput screening of activity/structures in small samples: many of these users would like to screen 200-300 samples per experiment, which is difficult with current measurement times and the oversubscription of instruments.

In the above areas, the length scales of interest span 1\AA - 1000\AA , so instruments with resolution options from $1\% \leq dQ/Q \leq 20\%$ are required. The thickest films from 500 - 100\AA requiring the highest resolutions are usually on solid supports however, and do not require a horizontal sample geometry. For the majority of purposes in specular reflectometry a Q-range of $0.005 - 0.5 \text{\AA}^{-1}$ is sufficient, and in cases where bulk liquid phases are part of the sample, the signal is typically background limited to below $Q = 0.25 \text{\AA}^{-1}$.

1.2 Description of Instrument Concept and Performance

1. Instrument layout and dimensions

A schematic layout of the instrument and its main components is shown from the side and from the top in Figure 4. The total length of the instrument is 25 m from the moderator. A 2.5 m supermirror guide with a constant height of 96mm begins at 2m from the moderator. The guide is rotated 1° around the x-axis (horizontal) and has an $m=6$ coating on the top face to deflect the beam down into the main guide, which is rotated at 2° down around the x-axis. The guide has elliptical top/bottom faces while the sidewalls are straight. The width of both the supermirror and elliptical guide is constant at 50 mm, and the height of the elliptical guide varies from 16-25 cm. The supermirror guide and the first 1.5m of the elliptical guide enclose a 4m-long multichannel bender with 7 vertical channels (0.5mm walls) and 56m radius of curvature. The black dotted lines in Figure 4a indicate the section of the guide up to 8.9m where the elliptical shape is not necessary and can be replaced by straight top and bottom walls, and another bender section if necessary. The elliptical guide is 15.5m long, and has a variable m-coating: 7.5% $m=5.45$ at each ends (2.3m), 20% $m=4.1$ section at both ends (6.2m) and a 7m $m=3$ section in the middle. The elliptical guide ends at 20m, and is followed by a 2m collimating guide with absorbing top and bottom faces. The beam incident on the horizontal sample is defined to the chosen angular resolution and footprint by two sets of precision slits located at 20m and 22m respectively. Immediately after the first collimation slit at 20m, a system of 3 fast shutters will select the angle of incidence for kinetic experiments. The shutter system is described in more detail in section 10. The sample position is located 5cm after the second focal point of the ellipse at 22.3m, and the sample to detector distance can be varied between 1 and 3m. If more space is required at the sample position for sample environments, this can be taken into consideration in the final design of the guide.

The instrument incorporates 8 choppers located at 6.5m, 6.7m, 7m, 8.5m, 10m, 11.1m, 15m and 15.6m from the source, whose function is described in detail in section 6. The radius of these choppers will be up to 750mm due to the large height of the elliptical guide (if the disc radius needs to be 3 x the guide height). The chopping is done from above across the 50mm width of the guide. The choppers have been drawn in Figure 4b) with a 750mm diameter (1000mm for FOC3) to illustrate the horizontal space requirements. The two dashed lines on the right panel in Figure 4b indicate 5° and 10° sectors around the beam port from which it is clear that 10° is required for this instrument. At the sample position same-level, side access to the sample area is necessary as many of the experiments involve relatively large (50-100kg) and delicate sample environments. A minimum width of 3m at the sample area is

envisaged. The detector will need to move both along the beam (3m) and vertically (1m), and have an evacuated flight path. This can be a cylindrical tank or a flight tube – the best engineering solution for this will be decided during the design phase.

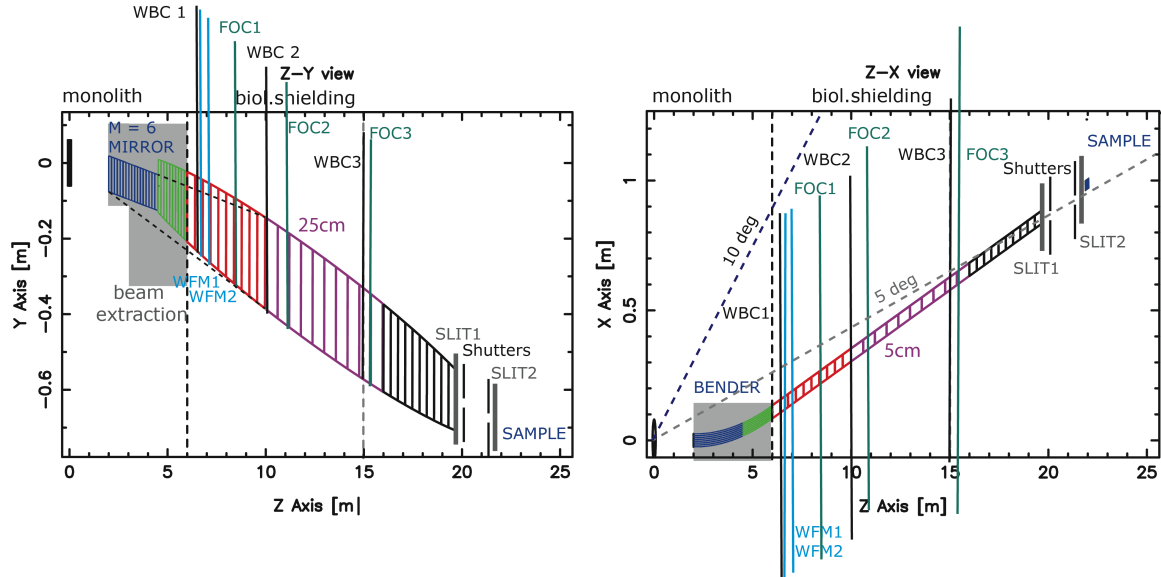


Figure 4. Schematic instrument layout – a) from the side and b) from the top indicating the position and relative size of the main instrument components. The chopper radii have been drawn in as simulated in panel b) (750mm, 1000mm for FOC3).

2. Time-distance diagram

At 25m, the usable wavelength band in the first frame is $2.5\text{-}11.3\text{\AA}$, as shown in Figure 5. The shortest wavelength was chosen considering the worst acceptable resolution (18.3% for 2.5\AA). If measuring across the prompt pulse is feasible, the wavelength band can be extended to 22.6\AA by skipping every second pulse.

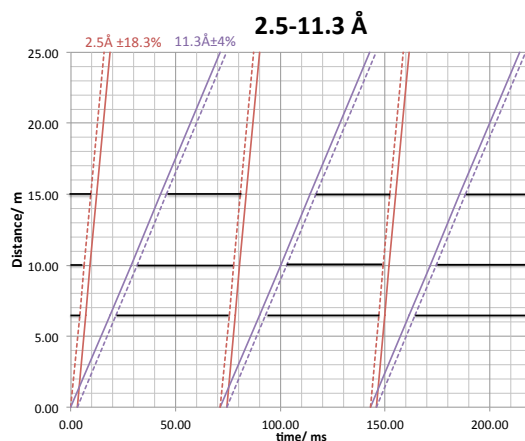


Figure 5. Time-distance diagram for a 25m instrument operating at 14Hz. The limiting usable wavelength was considered to be 2.5\AA with 18.3% resolution. The chopper openings shown were chosen so that the full pulse can be transmitted, which also includes shorter or longer wavelengths within the source resolution (shown as dashed lines).

3. How line of sight is avoided + shielding

The direct line of sight (LOS) to the moderator needs to be eliminated twice considering the likely high fast neutron background of the ESS. We started by optimizing a multichannel bender to transport 2Å neutrons and to provide two-fold LOS elimination (considering the channel width) before 6m.

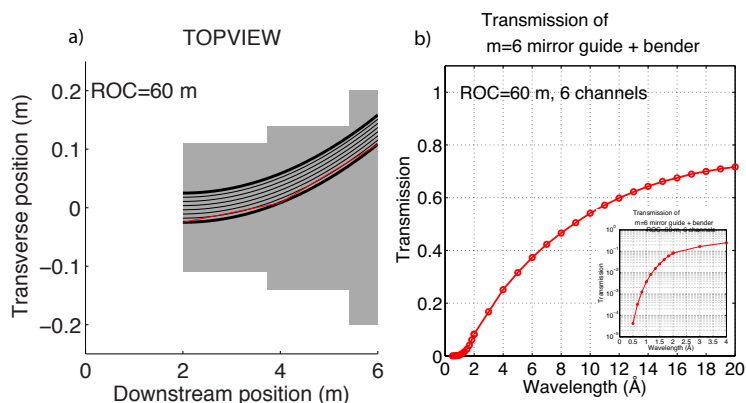


Figure 6 a) bender geometry inside the beam extraction unit for a 60m radius of curvature and 6 channels and b) the absolute transmission as function of wavelength.

Figure 6 shows the geometry of this bender inside the target monolith, as well as the absolute transmission of the supermirror + bender section as function of wavelength (not normalized to a straight guide transmission) for a radius of curvature of 60m and 6 channels separated by 0.5mm walls, with $m=5.1$ outer and $m=3.5$ inner surface coating.

The absolute bender transmission relative to the incoming intensity is shown in Figure 6b – if this is normalized against the transmission of an $m=1$ straight guide without channels, the transmission 48% for 2Å neutrons and it increases to about 70% for 20 Å neutrons. Since the bender characteristic angle is less than or equal to the critical angle of reflection for 2Å neutrons, their transmission is at least 67% compared to a straight guide with same number of channels and same m -coating, as expected (see Appendix for more details).

The maximum radius of curvature that can be accommodated with a 5cm guide in the beam extraction unit is 56m. This arrangement only provides line of sight elimination once if considering the full guide width, and due to this, a solution was suggested by the ESS optics group to insert another identical bender section after the first 3 choppers to extend the curvature to 10m from the source for two-fold LOS elimination. As the second bender section is relatively large (9.6-22cm tall), it is also expensive and discussions have already begun in order to find alternative solutions. These could involve reducing the guide width to 3.5cm, in which case a radius of 56m does allow LOS elimination twice before 6m, or using one or more solid-stated silicon benders. We will have been assured by the ESS optics group that the optimal solution can be developed during the design phase if the instrument proposal is accepted.

4. Neutron guide system and beam transport

The neutron guide system was optimised to deliver a broad divergence range and a broad wavelength band to the sample position, to enable measurements on liquid surfaces without moving the sample or the optics. An elliptical guide with $m=5.45$ at the first and last 7.5% of the guide length, followed by 20% of the length coated with $m=4.1$ and the middle 45% with $m=3$ is inclined at -2° relative to the horizontal, and delivers $\pm 2^\circ$ of divergence around the guide axis. Thus, an angular range of $0.2\text{--}4^\circ$ in the scattering plane is focused on the surface of the horizontal sample centred at 22.3m. The last 2m of the guide system comprise of a vertically absorbing collimating guide (between the two sets of collimating slits) that is designed to eliminate any parasitic scattering from the elliptical guide. Although a straight guide was simulated, a vertically tapering guide from the end of the elliptical guide (165mm) to 25mm at 22m can be used in reality. It is also in principle possible to replace this guide with horizontally focusing walls for small samples.

The instrument study was motivated by the need to find a sufficiently homogeneous distribution of flux over the full divergence range and the full wavelength band. For this, using an elliptical guide to directly extract the required divergence from the moderator would have been the optimal solution, but as the first 1.7m of the beam extraction unit has a restricted height (220mm), a 2.5m long supermirror inclined at -1° reflects the beam into the elliptical guide beginning at 4.5m from the source. This leads to somewhat larger gaps in the divergence profile, but does not affect the overall performance of the instrument. This, and the optimisation of the elliptical guide are explained in more detail in the appendix. Figure 7 shows the flux as function of wavelength and angle of incidence at the sample position. The gaps in the divergence originate partly from the mirror reflection and partly from the elliptical guide shape not being realised completely (only the fraction required to transport the full divergence was simulated). However, as explained in more detail in section 5, the full Q-range can be covered with sufficient flexibility in the choice of angles of incidence despite these gaps.

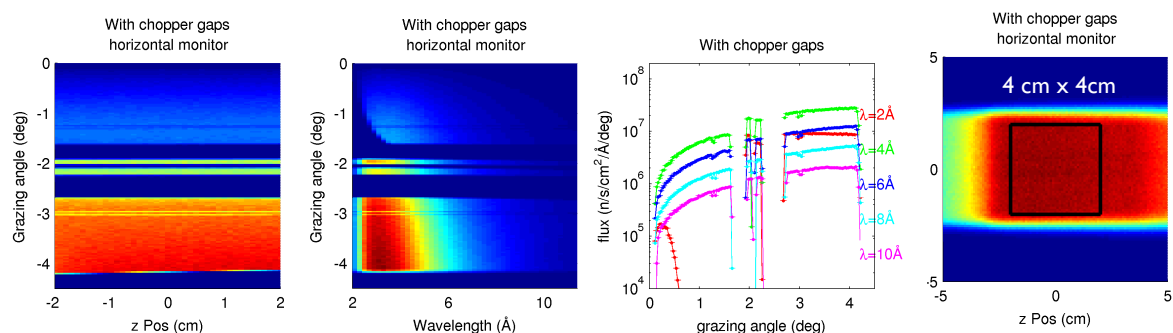


Figure 7. The angular distribution on a 4cm x 4cm sample area as function of sample length(z), wavelength, the full uncollimated intensity as function of angle of incidence, and full white beam footprint at the sample area, where the rectangle indicates a 4cm x 4cm area. The divergence profile includes reflections from both the top and bottom faces of the elliptical guide, as well as the straight through beam around the beam axis (-2°) originating from a reflection in the supermirror. The simulated guide included 5cm gaps for single disc choppers and 7cm gaps for the double disks in the locations listed in Table 1, section 6.

The guide system incorporates several choppers, and the required breaks in the guide could potentially lead to further beam losses or gaps in divergence. The effect chopper positioning was simulated for 5cm and 10cm gaps along the full guide length, and the result is shown in Figure 8. The end of the elliptical guide is more sensitive to the presence gaps, but for gaps of the order of 5cm-7cm (as estimated for single and double disc choppers for the ESS chopper group), the effect is negligible.

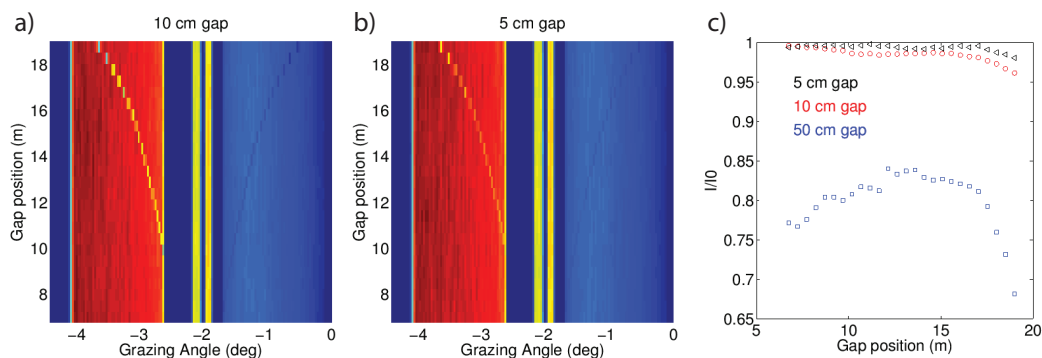


Figure 8. The effect of chopper gaps on the divergence delivered to the sample position as function of chopper position along the elliptical guide for a) 10cm and b) 5cm gaps. The effect on the total flux at the sample position is shown in c) for 5cm, 10cm and 50cm gaps.

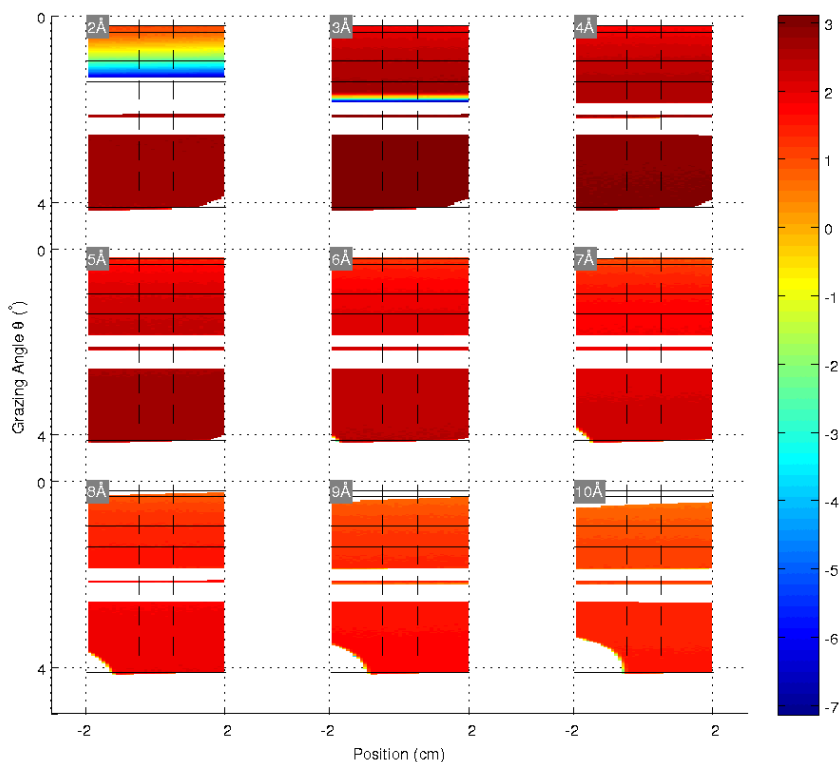
The instrument was optimised for 40mm x 40mm samples, which is considerably smaller than the sample sizes used for free liquid samples today (100mm x 30mm) or the average solid-liquid sample cells (80mm x 50mm). The right hand panel in Figure 7 shows the sample area illuminated by the fully open uncollimated neutron beam. As can be seen, a 4cm x 4cm sample can be fully and homogeneously illuminated, as well as longer samples up to 8cm if centred somewhat further forward from the nominal sample position.

Gravity was included in all the simulations, and for the 2.5-11.3Å band the effects on the vertical beam distribution are small. The collimating slit positions need to be adjusted to account for the parabolic neutron paths but the effect is small (<0.1mm). There is however some spreading of the beam footprint at the sample position, as shown in Figure 9 for wavelengths up to 10Å. The shift of the footprint occurs forward with increasing wavelength due to these being reflected later in the guide and at shallower angles. Wavelengths up to 15Å can be used if the sample is shifted 2cm further forward, and longer wavelengths up to 22.6Å can be used for longer samples (10cm). The footprints in figure 9 show that the beam is always completely homogeneous in wavelength, angle and flux within the central 1cm², indicating that the smallest sample size is only limited by the measurement times.

5. Used wavelength range(s), bandwidth and resolution as function of λ

At a detector position of 25m, the available wavelength band is 2.5-11.3Å within the first frame. The instrument has been optimised to function at 14Hz in a single frame mode, however, provided that measuring during the prompt pulse is possible, the wavelength band can be extended to 2.5-15Å, and up to 22.6Å for larger samples. The choice of wavelength band was based on the worst acceptable resolution (18.3% for 2.5Å) for thin films (<100Å), and the need for the broadest simultaneous Q-range. Figure 10 shows the full uncollimated beam flux on a 4cm x 4cm horizontal sample, and the wavelength resolution simulated at the detector position. The integrated flux on the 16cm² sample area is 1.84×10^8 n/s/Å/cm². The resolution is somewhat lower than predicted from the 2.86ms pulse width – e.g. for 6Å,

$d\lambda/\lambda$ is 8.08% (FWHM), as opposed to 7.6%. This results from the pulse tail during which neutrons are emitted at least up to 4ms from the cold moderator, and indicates that the effective pulse length for 6Å is 3.03ms.



1 9. Illumination of the sample area as function of wavelength and grazing angle showing the small forward shift with increasing wavelength.

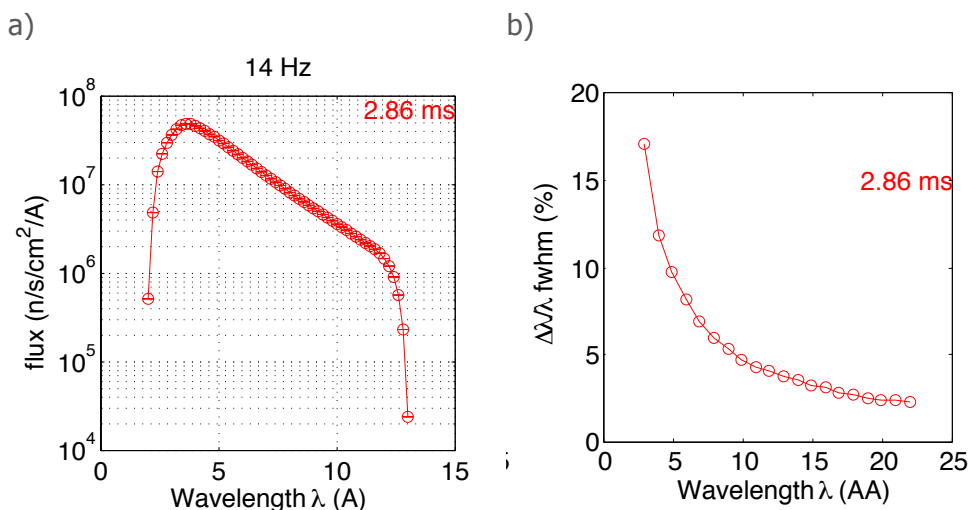


Figure 10. a) Simulated white beam flux on a horizontal 4cm x 4cm sample plotted as $n/s/\text{Å}/\text{cm}^2$ vs wavelength and b) the actual simulated wavelength resolution $d\lambda/\lambda$ (FWHM) at the detector position (for 7Hz/2 frames).

At 14Hz, the wavelength resolution ranges from 4% for 11.3Å to 18.3% for 2.5Å, which is not outside the resolutions used at existing instruments to increase the flux for high Q measurements.

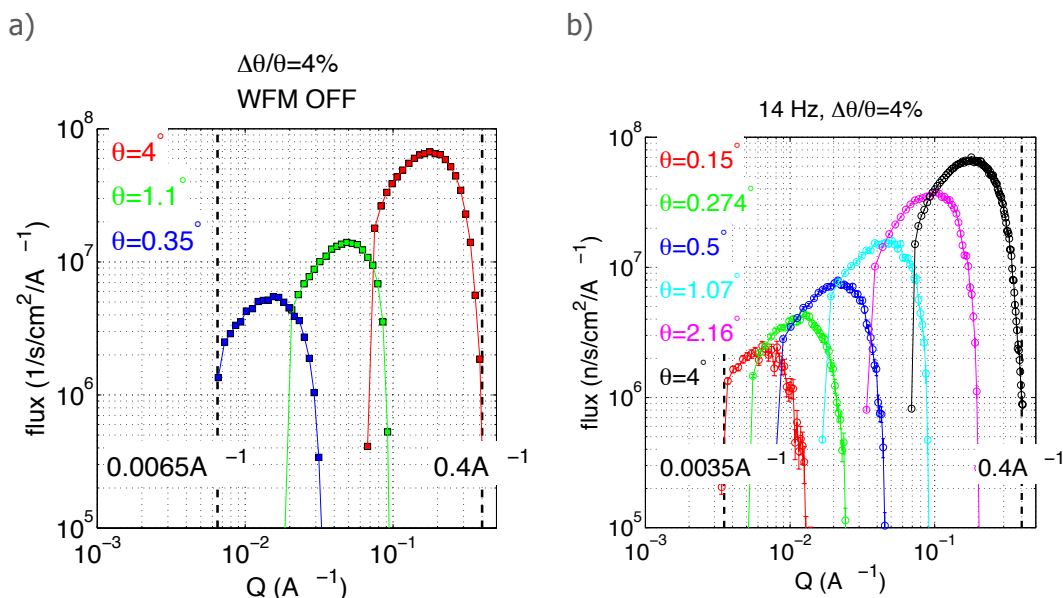


Figure 11. Collimated flux ($d\theta/\theta = 4\%$) as function of Q measured on a 4cm x 4cm horizontal sample a) using three angles of incidence and b) using 6 angles of incidence. The shortest wavelength included in the plots is 2.19Å.

Figure 10 shows that it is possible to cover the full Q -range of 0.0065-0.4 Å⁻¹ typically required for liquid samples in 3 angles with reasonable overlap ranges (0.01 Å⁻¹). Figure 11b) shows that the Q -range can be extended to cover 0.0035 < Q < 0.4 Å⁻¹, and gives an example of 5 angles of incidence selected from the divergence available. Higher Q -values are available by rotating the sample/detector for those samples that do not require a horizontal geometry. Thus, the natural resolution of the instrument can be used for a wide range of high flux experiments at medium to low resolution.

6. Choppers: how many, what is the layout and how do they work

The instrument includes two chopper systems:

- i) three wavelength band defining (WBC) choppers for using the natural resolution of the instrument with possibilities to vary the wavelength range and skip pulses.
- ii) 7-fold Wavelength Frame Multiplication (WFM) choppers for constant $d\lambda/\lambda = 2\%$

The chopping is in all cases done across the 5cm guide width, and preferentially from above the guide. The chopper locations, window heights, radii and frequencies are listed in Table 1.

The wavelength band and frame overlap chopper positions (shown in Figure 5) were optimised for allowing both 14Hz and 7Hz operations and to be compatible with the WFM chopper positions. Each WBC consists of a counter-rotating pair with variable opening, with the opening angles and times for 14Hz operations and 2.5-11.3Å shown in Table 1. 70Å was taken as the longest simulated wavelength for avoiding frame overlap. The third chopper at 15m is necessary for running at 7Hz. A vertical frame-overlap mirror could in principle be

used instead of the third chopper, but the chopper was considered to be a simpler solution than inserting such a vertical mirror inside the elliptical guide.

To increase the wavelength resolution, it is necessary to use WFM to preserve the usable bandwidth, as otherwise the bandwidth of the instrument is limited to 1.5\AA (due to the earliest possible chopper position being at 6.5m from the source). WFM relies on an optically blind chopper pair to create a sequence of short sub-pulses that are separated in time-of-flight but overlapping in wavelength, which allows a continuous wavelength spectrum to be used in data-reduction. The number of frames required to fill the frame is related to the ratio of the natural instrument length and the actual length of the instrument, with the number of frames increasing for short instruments. The natural length is defined as $L_{nat} = \text{posPS} + \text{posPS} * \tau / T$, where posPS is the distance of the WFM choppers from the source, τ is the pulse length and T is the source period. The WFM chopper system was optimised according to the method published by M. Strobl et al.¹

For FREIA, a constant $d\lambda/\lambda = 2\%$ can be achieved using 7-fold WFM as shown in Figure 12. In each frame, the shortest wavelengths originate from the end of the source pulse, and the longest from the beginning, with the selected pulse width being proportional to the wavelength, giving rise to constant $d\lambda/\lambda$. Each frame works in a manner analogous to a co-rotating double chopper pair operating with zero opening, with the resolution determined by the inter-chopper distance z_0 , which in this case is 0.364m . To avoid cross-talk between the sub-frames, and contamination from the source pulse tail (which extends to 5ms), 3 frame overlap choppers are required to keep the frames apart in time-of-flight until they reach the detector. Both the time between frames and the length of each frame become progressively shorter with increasing wavelength.

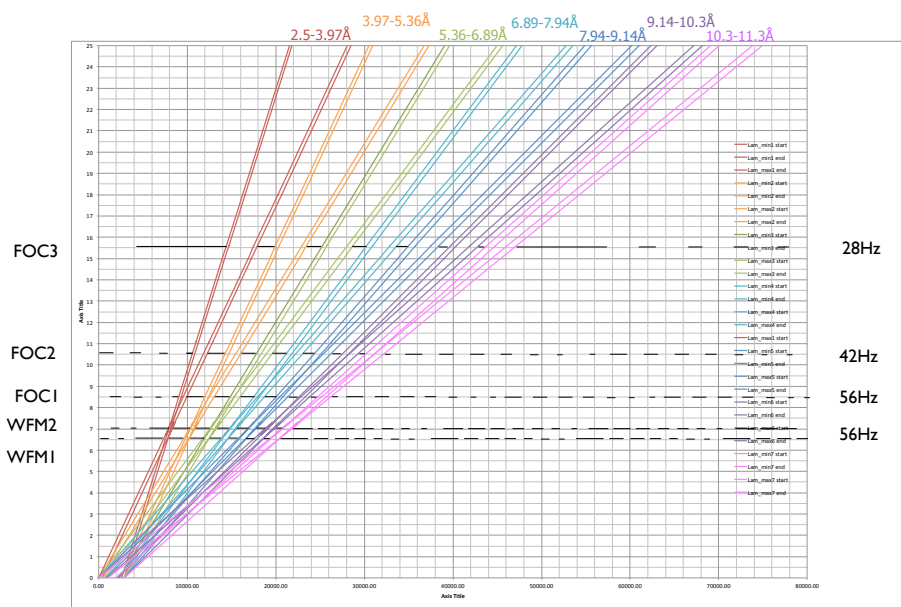


Figure 12. 7-fold wavelength frame multiplication for a 25m instrument at $d\lambda/\lambda = 2\%$ using wavelengths from $2.5\text{-}11.3\text{\AA}$.

¹ M.Strobl, M. Bulat, K.Habicht, Nuclear Instruments and Methods in Physics Research A 705 (2013) 74–84, doi: 10.1016/j.nima.2012.11.190.

MXType.Localized
 Document Number MXName
 Project Name <<project name>>
 Date 01/11/2013

Table 1. The final chopper configuration for FREIA showing chopper positions, opening angles, frequencies and disc sizes.

Chopper	Position/ m	Frequency/ Hz	Windows	Radius/ mm	Description
WBC1	6.5	14/7	1	750	Double disc
PSC1	6.713	56	7	750	Co-rotating pair
PSC2	7.074	56	7	750	
FOC1	8.5	56	7	750	Single disk
WBC2	10	14/7	1	750	Double disc
FOC2	11.1	42	7	750	Single disk
WBC3	15	14/7	1	750	Double disc
FOC3	15.6	28	7	1000	Single disk

The final chopper configuration and parameters are shown in Table 2, with Figure 13 showing the wavelength spectrum, time-of-flight of the subframes and the achieved wavelength resolution. In order to maintain pulse separation in time despite the slow chopper speed (28Hz) and the large guide cross section (5cm), the windows of the last frame overlap chopper FOC3 (at 15.6m) had to be reduced, as indicated in Table 2.

Table 2. WFM chopper configuration for 2.5-11.3Å, $d\lambda/\lambda = 2\%$.

Window	1	2	3	4	5	6	7
$\lambda/\text{Å}$	2.5-3.97	3.97-5.36	5.36-6.89	6.89-7.94	7.94-9.14	9.14-10.3	10.3-11.3
PSC1	7.32°	9.89°	12.34°	14.66°	16.85°	18.94°	19.98°
PSC2	7.32°	9.89°	12.34°	14.66°	16.85°	18.94°	19.98°
FOC1	17.95°	19.98°	21.91°	23.74°	25.47°	27.12°	28.68°
FOC2	27.88°	28.66°	29.41°	30.12°	30.79°	23.88°	32.03°
FOC3*	35.57°	34.06° (-3%)	32.13° (-7%)	28.61° (-15%)	26.26° (-24%)	24.31° (-24%)	31.48°

* The widows of FOC3 overlap chopper were reduced by the percentages given in brackets, in order to avoid frame-overlap.

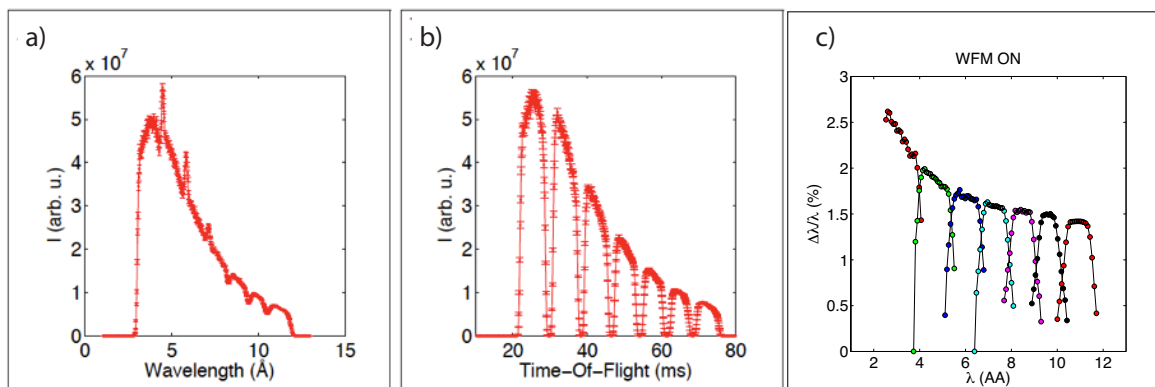


Figure 13. Simulated performance of the WFM choppers using the full guide system – a) wavelength spectrum and b) time-of-flight, simulated at the detector position. The small minima in wavelength are due to the window reduction of FOC3, c) actual $d\lambda/\lambda$ simulated at the detector position.

The resolution of the WFM chopper system shown in Figure 13c was determined from the time-of-flight spread of each wavelength at detector, with the wavelengths in each sub-frame determined from the simulated time-of-flight from the mid-chopper position to the detector. The details of how this was done can be found in the appendix. The achieved resolution varies between 1.5 and 2.5%. For the shortest wavelengths the resolution is somewhat worsened by the limited chopper speed. We will investigate during the design phase if it is possible to reduce the effect by a modification of the chopper windows. For the longer wavelengths, the resolution is sharpened due to the window reduction of the last frame overlap chopper in order to maintain frame separation in time.

7. +/- angular range and implications for moving sample/instrument

The FREIA guide system delivers an angular range of $+0.15$ - 4.1° divergence range on the sample position, which can be used without moving the sample. The slits are the only parts of the instrument that need to be moved to select particular angles of incidence. This gives rise to the a usable Q -range of $0.0035 < Q < 0.44 \text{ \AA}^{-1}$ for free liquid surfaces. For solid or enclosed liquid samples that can be tilted, a $0.5\text{m} \times 0.5\text{m}$ detector at 1m can be used to measure up to $2\theta=26^\circ$ without displacing the detector vertically, and at 3m up to 9.5° . It is likely however that a system to move the detector vertically will also be used.

Minimum Reflectivity (and how this is achieved for claims below 10^{-8})

This requires knowledge on the general background levels. We will aim to achieve $R = 10^{-7}$ on liquids, and 10^{-8} on solids.

8. Beam polarisation, guidefield, and analysis as function of λ

Polarising the beam was not part of the optimisation of FREIA, as the emphasis of the science case is on non-polarised studies. It is in principle possible to use a helium cell immediately before the sample position to polarise the beam, however this will not be an optimal solution for such a broad wavelength band. Likewise, using either a helium-based or a mirror analyser before the detector is possible, if required. However, we consider that as

99% of the samples that require polarised measurements are on solid substrates, they should be studied on a vertical reflectometer.

9. Measurements, data treatment and normalisation procedures

Data will be collected in event-mode, allowing the frames to be combined or rejected afterwards. Data-treatment will be done in the conventional way. Normalisation will ideally be done to monitors to account for any source fluctuations, which implies that several monitors with different efficiencies are likely to be necessary. Otherwise, a direct beam can be measured at each angle and slit setting. A solution to this will be determined during the first phase of the engineering design.

The instrument will have two operational modes. In the conventional mode, successive angles of incidence are recorded using the two sets of precision slits until sufficient statistics have been collected, and the data sets are combined. In the kinetic mode, three independent fast shutters will open and close three angles in turn, allowing background subtraction from each data set while spanning the full Q-range effectively at the same time, with the time-resolution of completing the cycle. The opening time of each shutter will depend on the experiment, but the design is aimed to allow opening for a single pulse at each angle, to allow measurements down to 71.42ms at one angle, and at 214ms for three angles. Three angles/shutters and pairs of precision slits have been chosen for practical reasons, as they allow a dynamic Q-range of up to 61.5 to be covered in the range between 0.0035 and 0.44 Å⁻¹, by combination of three angles in the ranges 0.15°-1°, 1-2° and 3-4.1°.

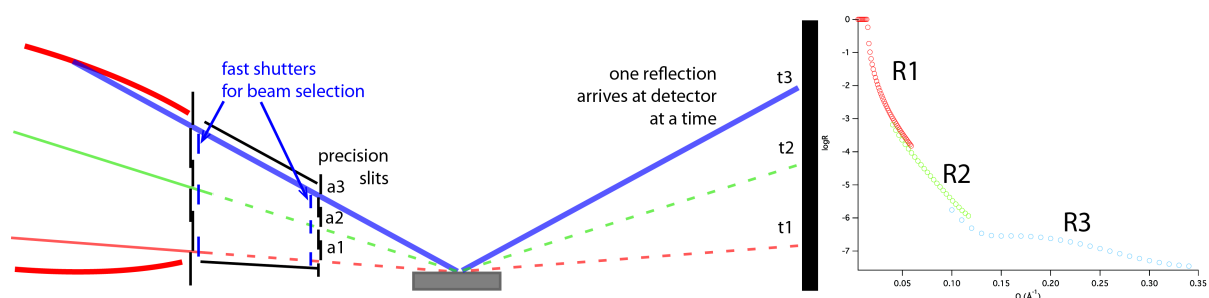


Figure 14. The operation of the instrument. Conventional measurements with data at each angle can be collected sequentially by opening and closing the three pairs of collimation slits in turn. The slits are each movable over a range and together cover the full angular range of the instrument. In the kinetic mode, fast shutters open and close each of the three slit pairs in turn, so that each pulse can arrive at the detector at a specific time and angle.

The slit system and fast shutters:

The three precision slit units will each have a variable opening and position. At 20m, the guide exit height is 165mm, but at 22m the full beam height is only 20mm and therefore the three slit pairs need to be mounted in a stacked fashion. It was considered that the slit positions should not be separated by more than 40mm along the beam direction in order to not change the angular resolution by more than 1% of its value (e.g. from 3.00% to 3.01%). Each slit pair will be designed for the required positioning and opening ranges - it is likely that for the angles below 0.3°, a special slit pair will be designed to provide a precision of 1µm, whereas the other slits only require a standard precision of 20 µm.

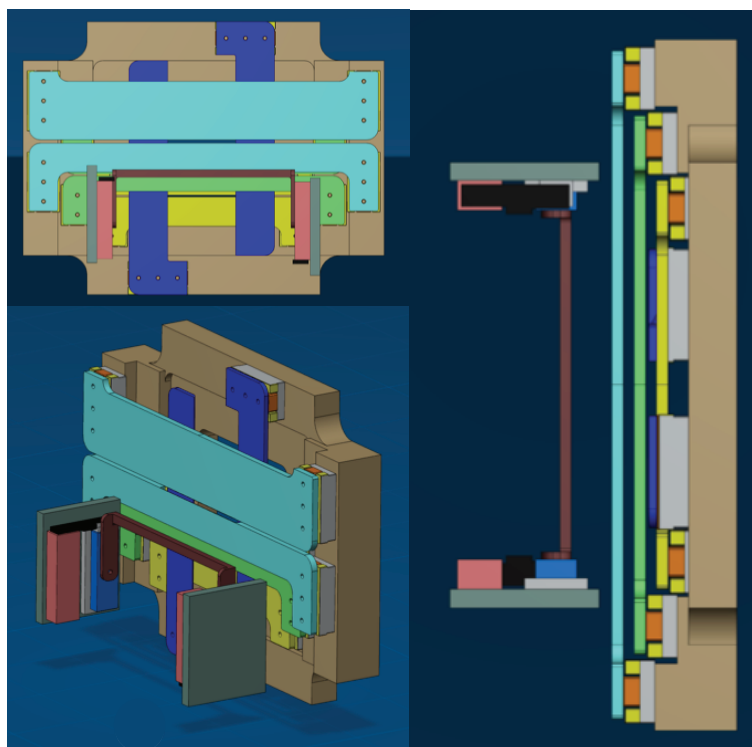


Figure 15. Preliminary engineering concept for the slit packages, shown for slit 2, which sits at 0.3m before the sample. Three pairs of precision slits and one vertical slit pair are mounted in a stack and are moved piezo positioners. A fast moving shutter blade is mounted before each opening, allowing independent opening and closing times.

The horizontal slit blades will each be driven by piezo positioners, with a common pair of vertical slits defining the beam width for all three angles. Such devices typically have a up to 30N capacity, minimum step size 0.1 μm , use a resistive encoder with a resolution of 0.1 μm and repeatability of 0.4 μm .

This shutter system will be designed to attenuate the beam to the same extent as the precision slits when they are fully closed, and to provide the minimum opening and closing times between pulses at the ms – timescale. Each shutter will operate independently so that a different opening time can be chosen for each angle according to the expected signal intensity from the sample, with the shortest opening time being one pulse period. The shutter blades could be driven by voice coils or linear piezo positioners, which have a typical resolution <5nm, repeatability < 1 μ and a build-in optical encoder with incremental with reference points (= absolute positioning possible). Such devices work well on synchrotron beamlines but have not been used in a neutron environment. The instrument budget includes 18 man-months for the design, manufacture and testing of this device.

10. Performance of instrument and virtual experiments using standard samples

The instrument performance was simulated using the full guide system and compared to FIGARO at ILL, which covers the same science case and has variable resolution. The full uncollimated flux on FREIA was measured to be 1.84×10^8 n/s/Å/cm² on a 4cm x 4cm horizontal monitor placed at the sample position, which represents the usable flux on a

MXType.Localized
Document Number MXName
Project Name <<project name>>
Date 01/11/2013

sample of this size. The total flux at the exit of the elliptical guide (5cm x 16cm) was determined to be 1.86×10^9 n/s/Å/cm².

Virtual experiments were carried out as agreed at a benchmarking meeting in December 2012. Each sample was simulated using the natural wavelength resolution, as well as with the WFM system with constant $d\lambda/\lambda = 2\%$, with selected examples shown below (all of the data is available on request). The samples were all simulated using an input data file (simulated in Motofit with 0.001% resolution, zero background and 25000 data points). The incoherent background was not included. The key parameters used were:

- 3Å roughness for all interfaces
- Sample size = this is the collimated illuminated area on sample (no overillumination) – it does not have to be square, as long as the area is constant
- Counting statistics: 50 counts in lowest statistics bin in the specular region (these points are represented by filled circles, whereas lower statistics points are given a dots)

Three angles of incidence (0.35°, 1.1°, 4°) were used to collect data in the theoretical Q-range of $0.0065 < Q < 0.4 \text{ \AA}^{-1}$, and in practise the Q-range was limited to obtain similar reflectivities to the experimental FIGARO measurements used for comparison. $d\theta/\theta = 4\%$ and the sample size was 40mm x 40mm in all cases.

The full list of samples simulated is:

SAMPLE 1. Air-D2O

SAMPLE 2. Air-Silicon with 15Å SiO₂ layer

SAMPLE 3. Si-SiO₂(15Å) - in D2O

SAMPLE 4. Air-null reflecting water (sld = 0) + 30Å monolayer with sld 4×10^{-6}

SAMPLE 5. Air-d-polystyrene (300Å, sld 4.5×10^{-6})-SiO₂(15Å)-Si

Figure 15 shows the reflectivity simulated from the air-D2O interface at the natural instrument resolution, and the actual resolution as function of Q. The simulated reflectivity reaches 2×10^{-7} in 2.05 seconds with similar statistics compared to the same data measured on FIGARO in 1 min. on a sample with approximately twice the area. The filled circles in Figure 15a represent data points with at least 50 counts – this data reaches up to 2×10^{-6} . The FREIA measurement is 29 times faster, and if taking into account the difference in sample size, 58 times faster.

One of the key design features of FREIA is to allow fast kinetic measurements on thin and weakly reflecting films at the air-water interface. Figure 16 shows data simulated from a 30Å deuterated monolayer (of e.g. a polymer or surfactant) on null-reflecting water in air. The estimated measurement time for all three angles down to 2×10^{-6} is 2.55 seconds.

Panel b in figure 16 shows the estimated time using only one angle of incidence in a limited Q-range to obtain the fastest possible time-resolution.

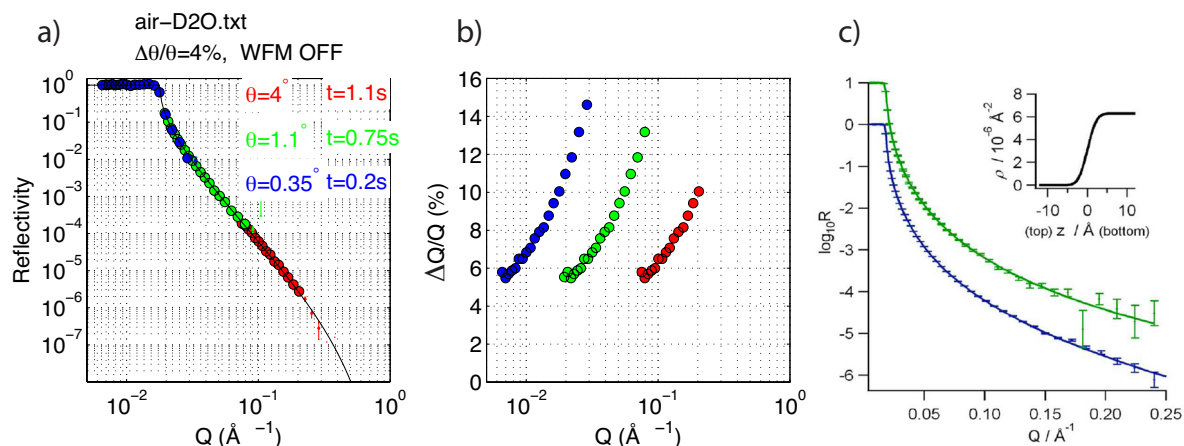


Figure 15. a) Simulated reflectivity from a 40 x 40 mm² air-D2O interface and b) the actual resolution on FREIA. c) shows data recorded with comparable resolution (7.25%) and statistics (green) on FIGARO in 1 min on a 40 x 80mm sample. The blue curve is measured on FIGARO in 40 min using $d\lambda/\lambda = 4.14\%²$.

The data reaches similar statistics to the example of 1s FIGARO data in 70ms (1 pulse), but the example shown to collect the requested statistics was simulated using 2 ESS pulses (140ms). The sample size in the FIGARO example is a 21Å monolayer with an sld of $6 \times 10^{-6} \text{ \AA}^{-1}$ giving rise to a very similar scattering contrast, but the sample area on FIGARO was 30 x 100mm². Taking the differences into account, the FREIA simulation is approximately 25 times faster.

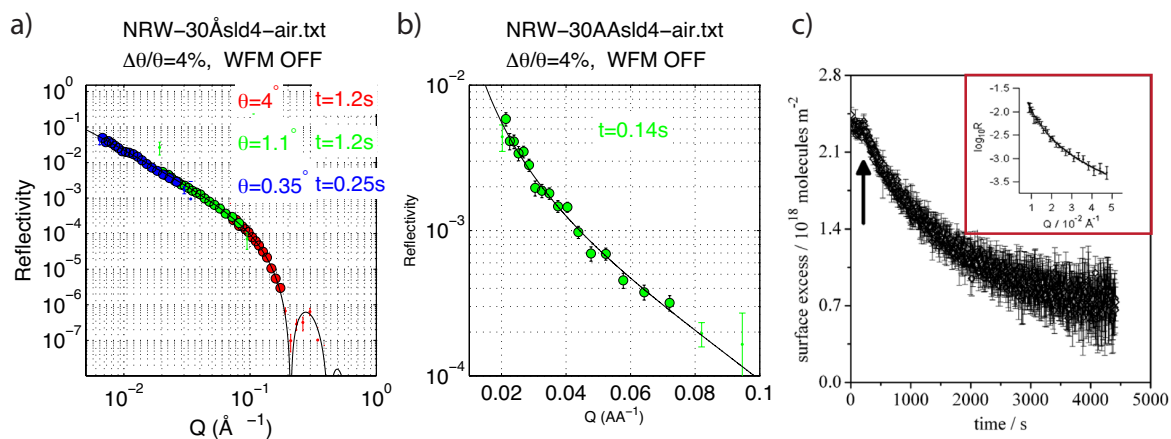


Figure 16. Simulated reflectivity from a 30Å deuterated monolayer (sld = $4.0 \times 10^{-6} \text{ \AA}^{-2}$) on null-reflecting water (sld = 0) – a) full Q-range simulated with three angles of incidence down to $R = 2 \times 10^{-6}$, b) the middle angle (1.1°) simulated in two pulses (140ms), and c) 1s data from FIGARO recorded at 0.68° with $d\lambda/\lambda = 7.25\%$ on a large sample (30 x 100mm²) of a similar reflectivity (15Å monolayer with sld $\sim 6 \times 10^{-6} \text{ \AA}^{-2}$).

² the FWHM of the resolution, corresponding to 74% of the full width resolution values published by Campbell et al. in Eur. Phys. J. Plus (2011) 126: 107 DOI 10.1140/epjp/i2011-11107-8. (private communication by P. Gutfreund)

The above two cases are examples where the measurable signal is limited by the incoherent background from the liquid sample ($1e^{-6}$ for D2O). Figure 17 shows the reflectivity from the air-silicon interface with a 15\AA SiO_2 layer simulated down to 10^{-7} to compare to routine measurement times for such data. The simulation times using both the natural wavelength resolution of FREIA (68 s) and 2% resolution (6 min 43.8s) are shown in comparison to data recorded at an intermediate resolution (4.14%) on FIGARO in 2 hours on a $5\text{cm} \times 8\text{cm}$ sample.

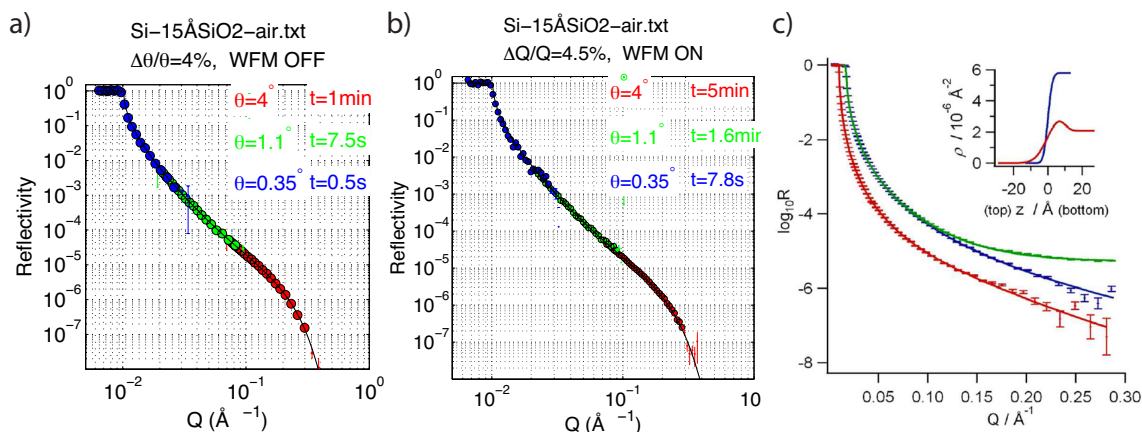


Figure 17. Reflectivity profiles of 15\AA SiO_2 at the air-Si interface a) at the natural FREIA resolution and b) using WFM ($d\lambda/\lambda = 2\%$) simulated down to $R = 10^{-7}$ and c) data measured on FIGARO (red curve) using $d\lambda/\lambda = 4.14\%$ in 2h.

The WFM system was incorporated into the FREIA design to allow higher resolution measurements on thicker films. As an example of this, data simulated from a 300\AA deuterated polymer layer (d-polystyrene, $\text{sld} = 4 \times 10^{-6} \text{\AA}^{-2}$) is shown in Figure 18 and compared to the same data simulated using the natural wavelength resolution. Panel c in Figure 18 shows the actual WFM resolution in the Q-range simulated.

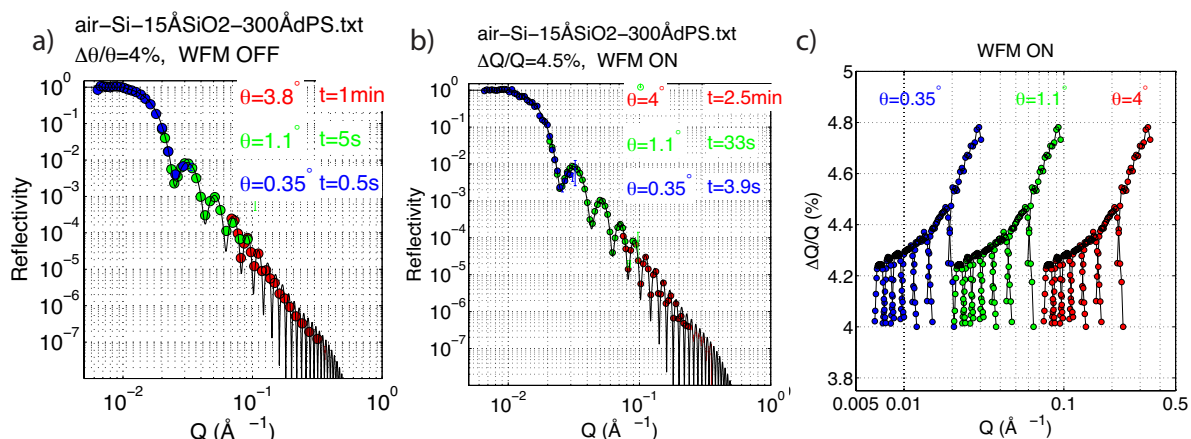


Figure 18. Reflectivity profiles of a 300\AA deuterated polystyrene layer on silicon (with a 15\AA SiO_2 layer) simulated a) without and b) with WFM, with c) showing the actual Q-resolution as function of Q.

MXType.Localized
Document Number MXName
Project Name <<project name>>
Date 01/11/2013

It can be seen from Figure 18a that the natural wavelength resolution of FREIA is only useful for measuring the first 3 interference fringes of the 300Å film, but also that the measurement times for the first two angles are an order of magnitude faster so that this could be used for fast kinetics of e.g. film swelling. With 2% wavelength resolution and at 4% angular resolution giving rise to 4.5% Q-resolution, the simulated time to reach 10^{-6} is 3 min 7s, and for the first two angles of the order of 30-40s which will be suitable for many kinetic phenomena that occur on longer timescales.

The 300Å d-polystyrene data was fitted in Motofit to the original reflectivity model using a constant resolution of 4.0%, as shown in Figure 19. This reflects the sharpening of the wavelength resolution of the longer wavelength by the modification of the frame overlap chopper windows, but could also include an effect from assuming a Gaussian peak shape in deriving the resolution. The somewhat worse resolution for the short wavelengths occurs over such a limited Q-range that it was not necessary to take it into account in the fitting.

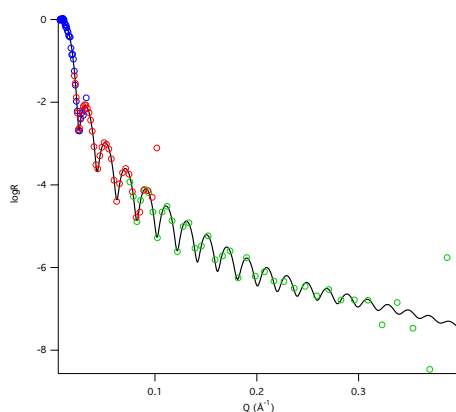


Figure 19. Simulated data from a 300Å d-polystyrene film on silicon (15Å SiO₂) fitted to the original reflectivity model using a constant $d\lambda/\lambda = 4.0$.

The virtual experiments above were all done with a 40mm x 40mm sample (because it takes a very long time to simulate smaller samples), but considering that the flux and wavelength distribution are completely uniform within the central 1cm² area (see Figure 8), the measurement times for samples smaller than this should scale with the illuminated area. Thus, it should be possible to measure a 1cm² air-D₂O sample in $16 \times 2.05s = 32.8s$, and a 1cm² d-polystyrene sample on silicon at 2% resolution in 49.8 min. Samples smaller than this will be possible, and it should be possible to measure a 5x5mm² air-Silicon sample to 10^{-7} without WFM in 72.5 minutes.

For any samples that do not cause a significant off-specular background, it should also be possible to use FREIA in a wide-divergence mode similar to the Estia concept, particularly by using sections of the full 4 degree divergence to extend the simultaneous Q-range at one angle. These options will be investigated in full during the design phase as they also depend on developing a more detailed concept for the slit packages and shutters, and the count-rate capabilities of the detectors available.

To summarise, the virtual experiments show that FREIA is applicable to a variety of samples and can be used at both resolutions with significantly faster measurement times than on existing instruments. The uniform flux on sample allows for both small and larger samples to be investigated, and more advanced measurement options using e.g. wider divergence are possible.

MXType.Localized
Document Number MXName
Project Name <<project name>>
Date 01/11/2013

11. Functional detector specifications

This instrument can use existing technologies, e.g. a 0.5m x 0.5m ^3He -tube detector with 1mm x 8mm resolution, and the price of this detector is not expected to be significantly different to a ^{10}B detector, therefore in the costing only a general estimate obtained from the ESS Detector group was used. The boron technology could however offer an advantage, as it could have enough energy resolution (due to the absorption depth of different wavelengths) to discriminate the inelastic incoherent background from water. The most important criterion for the FREIA detector is the count rate capability, because the direct beam neutron flux can reach 10^8 n/s on a relatively small area (e.g. 5mm x 500mm).

12. Off-specular and GISANS q-ranges/resolution and how they are achieved

This instrument is intended to function as a specular reflectometer, with some off-specular capability. At this stage no GISANS collimation is planned - although it is possible in principle, it will not use the flux available on the instrument in an optimal way.

13. How are GISANS and/or SERGIS modes implemented in practise? N/A

14. Do you need to measure during the prompt pulse, and what is the cost if you can't?

We have followed the advice from the ESS Optics group and can go out of line of sight of the moderator twice using eventually two multichannel bender sections. We have been assured that having done this, the prompt pulse should not present problems. However as reflectometry is a very background sensitive technique, we have considered it necessary to ensure that the instrument is fully functional and will cover its science case using only the first frame. In the event that data cannot be data acquired during the proton pulse, the instrument can still be used to record data with the longer wavelengths by either working only in the second frame or by recording one additional angle of incidence to cover the gaps for the prompt pulse duration in a pulse skipping mode.

15. Feasibility/risks of any new or non-standard components

The main risk as perceived today relates to the size requirements for the WFM choppers PCS1 and PSC2. Informal discussion with Astrium representatives have not identified any insurmountable difficulties.

The second feasibility question relates to the fast shutter system. The ESS motion control group has welcomed the challenge of designing a concept, and the preliminary work suggests that a solution can be developed to allow each angle to be operated by an independent shutter. We expect to test and prototype this system as part of the design phase, and have included 6+12 months of engineering time for this purpose, as the component is specific to FREIA. It should be noted that the instrument will function as well as any other liquids reflectometer (still without having to move the sample) with the ability to record the whole Q-range sequentially, even if the development time for this system needs to be extended and it is not available on day 1.

MXType.Localized
Document Number MXName
Project Name <<project name>>
Date 01/11/2013

16. Optics and assumptions made – define reflectivity for m-coatings etc.

The simulated guides are built of either the component testcomp49.comp written by Henrik Carlsen and Mads Bertelsen or guide_gravity. Gravity is included in the simulations. The optimization of the guide system was conducted within the iFit Data Analysis library written by E. Farhi (<http://ifit.mccode.org/>). An analytical equation fitted to reflectivity curves from Swiss neutronics was used describe the reflectivity of multilayer mirrors (see appendix).

For the elliptical guide components, the same m-coating had to be simulated for both side and top/bottom walls in each section, although in reality the side walls can have a lower m-coating.

17. What are the tolerances? When does instrument no longer work? (due to e.g. guide quality, if WFM is not possible etc.)

It was suggested that the instrument may suffer in terms of the quality of the divergence profile due to misalignment of the elliptical guide sections – we however believe that we have answered this question during the investigation of the effect of guide breaks for choppers, as misalignment of the guide pieces would have a qualitatively similar effect. The observed divergence gaps are negligible up to 10cm gaps.

If the WFM system is not found feasible due to the mechanical constraints of the components, the instrument will function well in the high-flux mode for thin films and fast kinetics and reach higher resolutions in the second frame. Although this depends somewhat on the ability to use the frame-overlap neutrons, the instrument will be still applicable to many kinds of samples where $\langle d\lambda/\lambda=7.6\% \rangle$ is sufficient, as the lowest resolution data can in the vast majority of cases be discarded.

If the fast shutter system proves to be impossible, or is delayed, the instrument will function as a high flux liquids reflectometer with the ability to record the whole Q-range sequentially still without moving the sample and for non-liquid samples, some of the divergence may be used simultaneously in a fashion similar to the Estia concept.

1.3 Technical Maturity

Bender section: This is relatively large and expensive – the design has been simplified as the elliptical top and bottom faces are not necessary, and can be replaced by a trumpet. During the design phase, alternative solutions such as solid-state silicon benders will be investigated as a more compact and economical solution.

Elliptical guide: This is not used for point-to-point imaging as in the case of the Selene guide concept, and as such its performance is less sensitive to guide misalignments. Off-specular scattering will be removed by the two slits and collimating guide.

Choppers: The performance requirements are clear from the simulation study. All of the discs are relatively large due to the large guide size, and there are two particularly fast choppers with 7 windows of variable size. Advice has been sought informally from Astrium, who have not indicated that this will be a problem. The engineering solution to this will need early attention during the design phase.

MXType.Localized
Document Number MXName
Project Name <<project name>>
Date 01/11/2013

Fast shutters: Advice has been sought from both electrical and mechanical engineers at ESS. Suitable technologies for exist, but this system will require development. An estimate for the development and prototyping time (18 months) is included in the Design phase.

1.4 Costing

The costing is presented in detail in Table 3. Hardware costs generally include components, manufacturing, testing and installation. Most of the costs will be incurred in the Procurement and Installation phases, but some of the major procurements may be initiated in the Final Design phase by decision of the Chief Instrument Engineer. This cost estimate should be regarded as very preliminary and only indicative of the relative cost profile between the various components. The manpower is estimated in person-months (10 k€/month) and the following categories are included:

Integrated Design: Overall instrument design by the Lead Scientist and engineer, as well as other scientists and engineers involved.

Systems Integration: Systems engineering for compatibility between components and compliance with ESS standards.

Detectors and Data Acquisition: Detector system including electronics. The cost estimate, which includes electronics, beam monitors, and the design work/installation, is based on discussions with the ESS Detector group.

Optical Components: The beam delivery system including the bender, guides, guide housing and alignment system, collimation slits and the fast shutter system. The guide cost estimate of 500k€ is based on a confidential market survey by the ESS Neutron Optics group, assuming that the guide has the same m-coating for all four sides. For the 4+4m bender a quote of 1.94M€ was obtained from Swiss Neutronics as the upper limit for the cost of going out of line of sight twice. The estimate for the slit package and shutter development (100k€ hardware) given by the ESS Motion control and project engineering group also contains 18 person-months to test and prototype this novel system during the Design phase.

Choppers: The estimate from the ESS Chopper group includes all motors, vacuum housings and other infrastructure to operate the choppers.

Detector Vessel: The vacuum vessel (3.5m) for the detector, including pumps, windows, mounting and installation.

Sample Environment: Goniometers, rotation and translation stages for mounting samples and specific sample environment such as liquid troughs, flow cells, sample changers, controlled atmosphere boxes etc.

Shielding: Shielding for radiation protection and background reduction, including shutter systems. The estimate is based on guidelines from the ESS Optics group (1.5 times the cost of the guide system, estimating a straight guide with the same m in place of the bender).

Instrument Specific Support Equipment: This includes mechanical components not costed elsewhere.

Instrument Infrastructure: The buildings and facilities not provided as part of the Conventional Facilities budget, such as cabins, mezzanines, raised floor areas etc. As no definite floor plan exists at the moment, the estimate here is based on information from last year's instrument proposals.

MXType.Localized
 Document Number MXName
 Project Name <<project name>>
 Date 01/11/2013

in k€	Phase 1 (Design and Planning)			Phase 2 (Final Design)			Phase 3 (Procurement and			Phase 4 (Beam Testing and Cold			Total			
	Hardware	Staff (k€)	Staff (months)	Hardware	Staff (k€)	Staff (months)	Hardware	Staff (k€)	Staff (months)	Hardware	Staff (k€)	Staff (months)	Hardware	Staff (k€)	Staff (months)	Staff (Years)
Integrated Design	0	420	42	100	720	72	0	480	48	0	240	24	100	1860	186	15.50
Systems Integration	0	0	0	0	30	3	0	120	12	0	60	6	0	210	21	1.75
Detectors and Data Acquisition	0	60	6	0	60	6	1200	30	3	200	120	12	1400	270	27	2.25
Optical Components	0	60	6	0	60	6	2500	30	3	20	60	6	2520	210	21	1.75
Choppers	0	60	6	100	60	6	2500	30	3	50	30	3	2650	180	18	1.50
Detector Vessel	0	30	3	0	30	3	1000	30	3	0	10	1	1000	100	10	0.83
Sample Environment	0	0	0	0	30	3	500	10	1	200	60	6	700	100	10	0.83
Shielding	0	30	3	0	60	6	2250	60	6	20	60	6	2270	210	21	1.75
Instrument Specific Support Equipment	0	0	0	0	30	3	100	120	12	20	30	3	120	180	18	1.50
Instrument Infrastructure	0	30	3	0	30	3	100	60	6	20	30	3	120	150	15	1.25
Total	0	690	69	200	1110	111	10150	970	97	530	700	70	10880	3470	347	28.92
Grand total (no VAT)	14350															

Table 3. Instrument construction budget

MXType.Localized
Document Number MXName
Project Name <<project name>>
Date 01/11/2013

2. LIST OF ABBREVIATIONS

Abbreviation	Explanation of abbreviation
--------------	-----------------------------

WFM	Wavelength frame multiplication
------------	--

WBC	Wavelength band chopper
------------	--------------------------------

FOC	Frame overlap chopper
------------	------------------------------

PNR	Polarised neutron reflectometry
------------	--

LOS	Line of Sight
------------	----------------------

NR	Neutron Reflectometry
-----------	------------------------------

PROPOSAL HISTORY

New proposal:	(yes/no)
Resubmission:	(yes/no)

APPENDIX: FREIA

Anette Vickery and Hanna Wacklin

October 31, 2013

Contents

1	Instrument layout and dimensions	2
2	How direct line of sight of the guide entry is avoided	4
2.1	Reflectivity	4
2.1.1	Critical angle of reflection	4
2.1.2	Reflectivity model for a supermirror	4
2.2	Curved neutron guide, bender	5
2.3	Bender design	5
3	Neutron guide system and beam transport	6
3.1	Loss of neutrons in the mirror guide and bender	6
3.1.1	Mirror guide transmission	7
3.1.2	Estimated loss due to bender channels	9
3.1.3	Estimated loss due to bender curvature	9
3.1.4	Summary	10
3.2	Loss of neutrons in the elliptical guide	10
4	Used wavelength range	10
4.1	Estimated available Q-range	10
5	Virtual experiments using standard samples	11
5.1	Estimation of counting times and realistic errorbarsxs	11
5.2	Conversion of time-of-flight WFM data	11
5.3	Derivation of Q-resolution from simulated data	13

6	Optimization using McStas	13
6.1	The optimization strategy	13
6.2	optimizing the distribution of intensity vs grazing angle at the sample position	13
7	Comparison of McStas 1.12c and McStas 2.0 simulated results	14
7.1	Differences in instrument layout and consequences for the flux distribution . .	14
7.2	Sample flux comparison	15
7.3	Summary	16

1 Instrument layout and dimensions

The neutron guide system aims at focusing a neutron beam with wavelengths in the range $2 \text{ \AA} - 10 \text{ \AA}$ to a focal spot at the sample position. We expect that an elliptical or parabolic shaped guide with one focal point coinciding with the sample position can transport to the sample position a wide range of grazing angles and wavelengths with high intensity due to only one reflection in the guide. It is estimated that the achievable angular range has a width of approximately 4 times the critical angle of reflection α_c for the shortest wavelength (2 \AA). Depending on the realizable mirror coating, this amount to $2.8^\circ - 4.75^\circ$ ($m = 3.5 - m = 6$), see also Sec. 2.1.1. Ideally the angular range should extend from 0° to $4\alpha_c$, hence the guide optical axis must have an inclination corresponding to the center of the angular range. In Fig. 1A the red dashed line indicates the optical axis of such an optical element: the inclination is 2.14° relative to horizontal and it passes through the center of the moderator face. Clearly, the layout of the beam extraction unit does not allow space for such an optical element.

The pair of parallel black lines in Fig. 1A indicates the top and bottom of a guide segment inclined by 1.14° . The dashed blue line is inclined by 2.14° and passes through the guide top center. So if the neutrons are deflected by that mirror into an elliptical guide with the blue dashed line as an optical axis, the guide system (mirror+elliptical guide) can fit within the beam extraction unit. Fig. 1B shows a sideview of the proposed guide system. The ellipse has a minor axis of 25 cm and an optical axis inclined by 2.14° . Here, the dashed blue line, which is coincident with the deflection mirror, intersects the upper wall of the ellipse at 8.9 m from the moderator. The green and black dashed lines show rays with wavelengths 2 \AA and 3.3 \AA respectively, critically reflected off the mirror ($m = 6$). This guide solution has 2 drawbacks compared to the solution without the mirror: 1) the majority of the neutrons reaching the sample position are reflected one more time (in the mirror). However, the neutrons are already reflected many times in the side walls of the guide system, so for the longer wavelengths ($> 3.3 \text{ \AA}$) the extra reflection in the mirror will not have a noteworthy impact on the total flux reaching the sample position. 2) due to the critical angle of the mirror, the very low wavelengths (between 2 \AA and 3.3 \AA) can only partly illuminate the lower part of the ellipse. The rays reflected off the lower part of the ellipse are incident on the sample position with angles less than the inclination of the optical axis (2.14°). This issue is addressed in Sec. 4.1. In Sec. we outline the method of optimization using McStas.

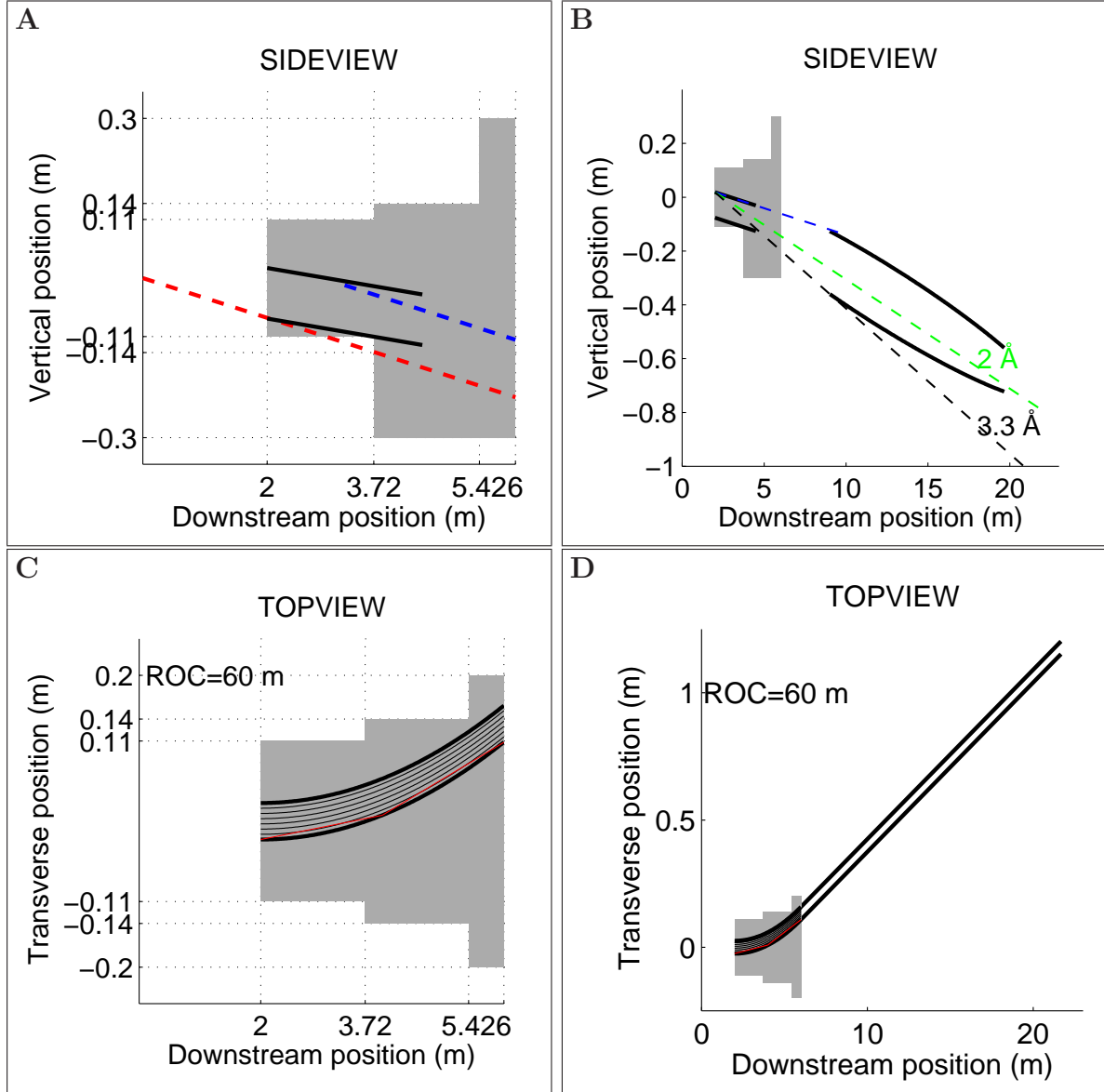


Figure 1: Drawings of the baseline beam extraction unit (2 m to 6 m downstream the moderator) and the proposed guide system. The optical elements positioned closer to the moderator than 6 m downstream must fit within the grey area.

A: SIDEVIEW. The red line indicates the optical axis of an elliptical guide with an inclination 2.14° (corresponding to 2 times the critical angle of 2 \AA neutrons ($m=5.4$)). Clearly the beam extraction unit constrains the space so there is not room for an inclined elliptical guide this close to the moderator. The black lines indicate the position of a deflecting guide element with an inclination of 1.14° (corresponding to the critical angle of reflection for 2 \AA neutrons, $m = 5.8$). The blue dashed line indicates the optical axis of an elliptical guide capable of transporting the beam reflected off the mirror. Clearly such an elliptical guide can fit within the beam extraction unit. The elliptical guide entrance is at 8.9 m from the moderator face. Between 6 m and 8.9 m there is no need for a guide with reflecting top/bottom, therefore this is not included in this drawing.

B: SIDEVIEW. The blue dashed line indicates the paths of rays entering the guide along the mirror surface. This line intersects the elliptical guide at 8.9 m from the moderator. The green dashed line indicates the critical angle of reflection for 2 \AA neutrons (1.19° , $m = 6$). This line shows that the 2 \AA neutrons are not reflected from the lower part of the ellipse. The black dashed line indicates the critical angle of reflection for 3.3 \AA neutrons ($m = 6$). The line intersects the lower part of the ellipse at the ellipse entry. Therefore, neutrons with wavelenths in the range $2 \text{ \AA} - 3.3 \text{ \AA}$ will only partly illuminate the lower part of the ellipse.

C: TOPVIEW. To avoid the direct line of sight of the guide entry the first 4 m of the guide system is combined with a 6 channel bender of width $W = 5 \text{ cm}$. The channelwidth is then less than 8.33 mm, - how much depends on the realizable bender wall thickness. The radius of curvature is 60 m. If the bender walls are infinitely thin, direct line-of-sight length is 2 m, so the 2nd extreme 'Garland' reflection takes place at 6 m from the moderator face. The red line indicates a ray which is incident on the outer bender wall with the characteristic angle $\theta = \sqrt{2w/ROC}$ where w is the bender channel width.

D: TOPVIEW. The side walls of the guide are straight with a width of 5 cm. The sample position is at 22 m from the moderator.

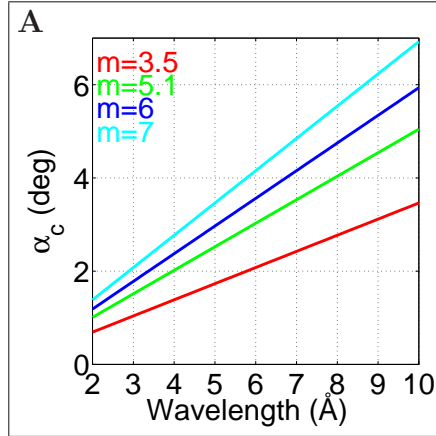


Figure 2:A: The critical angle of reflection for different m values.

2 How direct line of sight of the guide entry is avoided

The simulated instrument has the mirror guide and the first 1.5 m of the elliptical guide included in a 7 channel bender with radius of curvature 56 m. If we only account for the width of the bender channels, this 4 m bender section eliminates twice the direct line-of-sight of the guide entry. However, considering that the fast neutrons will penetrate the bender channel walls, we have to account for the total guide width of 5 cm when calculating the line-of-sight length. In Sec. 2.3 is outlined a new bender design which is not yet implemented in the instrument simulations. Sections 2.1 and 2.2 contain a short explanation of the theory which forms the base of Sec. 2.3 .

2.1 Reflectivity

2.1.1 Critical angle of reflection

The reflectivity drops to 67% at the critical angle of reflection. Assume that a mirror has a critical scattering vector of length $m Q_{Ni}$ ($Q_{Ni} = 0.0217 \text{ \AA}^{-1}$). For neutrons with wavelength λ the critical angle of reflection is

$$\alpha_c = \frac{m Q_{Ni} \lambda}{4\pi}. \quad (1)$$

The critical angle of reflection is proportional to the neutron wavelength, and in general, for realizable m values, $\alpha_c < 2^\circ$ for $\lambda < 2 \text{ \AA}$. Figure 2A shows the critical angle as function of wavelength for different values of m .

2.1.2 Reflectivity model for a supermirror

The simulations utilize an analytical model for the reflectivity R of a supermirror with critical scattering vector of length $m Q_{Ni}$:

$$R = R_{Ni} - \alpha(Q - Q_{Ni}) \quad \text{for } Q > Q_{Ni}, R = R_{Ni} \quad \text{for } Q < Q_{Ni}, \quad (2)$$

where $R_{\text{Ni}} = 0.98$, $Q_{\text{Ni}} = 0.0217 \text{ \AA}^{-1}$ and

$$\alpha = 0.1 \frac{m - 2}{Q_{\text{Ni}}(m - 1)} \quad \text{when } m > 2, \quad \alpha = 3.2 \quad \text{for } m > 2. \quad (3)$$

Figure 4C shows Eq. 2 for $m = 5$ and $m = 6$.

2.2 Curved neutron guide, bender

Theoretically, a straight neutron guide with a rectangular cross section that is fully illuminated by the source will transmit a beam with a square divergence of full width $2\alpha_c$ in both the horizontal and vertical directions, that is the transmitted solid angle is proportional to λ^2 , see Eq. 1. In general, there are two possible types of reflection, called garland and zig-zag reflections. Garland reflections involves the outer wall of the curved guide only, whereas zig-zag reflections are reflections off both inner and outer walls, alternately. Fig. 3A shows a segment of a curved neutron guide with a rectangular cross section and width w . The arrow indicates the flight path of a neutron which is garland reflected with the characteristic angle

$$\theta^* \approx \sqrt{2w/R} \quad (4)$$

of reflection, that is the maximum angle under which garland reflections can take place. Note that if $\theta^* > \alpha_c$ neutrons are transmitted by garland reflections only. The direct line-of-sight length is

$$L^* = 2R\theta^* = \sqrt{8wR} \quad (5)$$

The line-of-sight length can be reduced by subdividing the guide into a number of narrower channels, each of which acts as a mini-guide. The resulting device is often referred to as a neutron bender. Fig. 3B compares the transmission of a bender to that of a straight channeled guide of same length and with same coating. When $m = 4.1$ we have $\theta^* = \alpha_c$ for 2 \AA neutrons and the transmission drops to 67% of that of a straight channeled guide. With $m = 5.1$ the transmission of 2 \AA is 80% due to the transmission of additional zig-zag reflections. These results are in agreement with¹.

2.3 Bender design

This section describes the analytical calculations behind the latest bender design. These calculations are based on Sections 2.1.1 and 2.2. Sec. 2.1.1 describes the reflectivity curves for a supermirror with critical scattering vector mQ_{Ni} for different values of m . In Sec. 2.2 the expressions for the bender characteristic angle θ^* and the line-of-sight length L^* are derived (in accordance with the ILL neutron data booklet) as function of bender radius of curvature R and channel width w .

The minimum radius of curvature is limited to 56 m by the baseline design of the beam extraction unit Fig. 1C. With a guide width of 5 cm, the direct line-of-sight length is calculated by Eq. 5 to $L^* = 4.73 \text{ m}$. Therefore, one way of eliminating twice the direct line of sight of

¹ILL Neutron Data Booklet, Second Edition

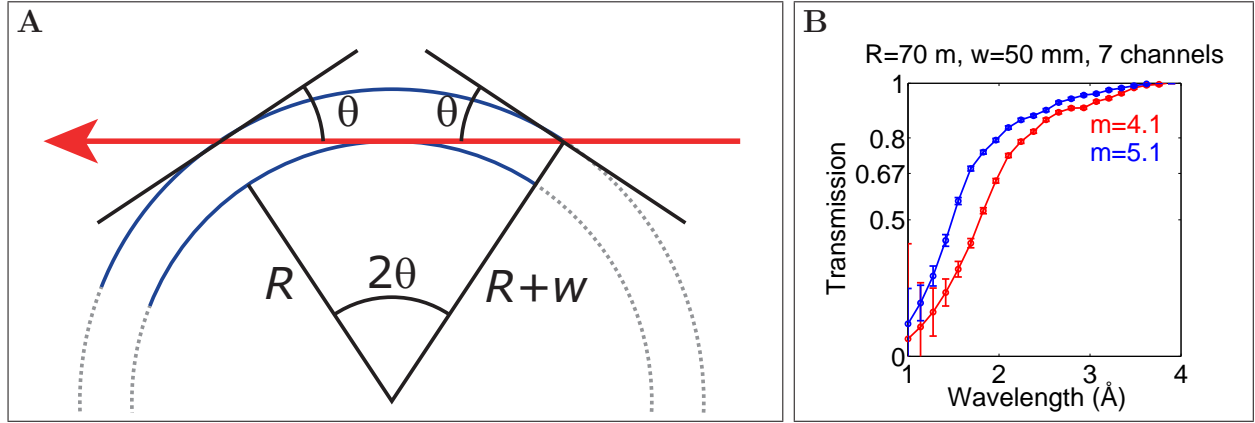


Figure 3:

A: The arrow indicates the flight path of a neutron entering a curved guide with width w . The guide curves to the left with the radius of curvature R . Here we consider the limiting case, where the neutron just glances of left wall. Due to the curvature, the neutron will hit the right wall at an angle θ . From the sketch it is clear that $\cos \theta = R/(R+w) \approx 1 - \theta^2/2$, and therefore $\theta \approx \sqrt{2w/R}$. The length of the corresponding scattering vector is $q = (4\pi/\lambda)\sqrt{2w/R}$. To scatter the neutron, we need $q \leq mQ_{c,\text{Ni}}$, so the shortest wavelength which can be transported by the guide is $\lambda_{\min} = \frac{4\pi}{mQ_{c,\text{Ni}}} \sqrt{\frac{2w}{R}}$. The neutron is reflected at the distance $R2\theta$ from the guide entrance. The transmission of a bender relative to straight guide segment with the same coating and number of channels.

B: The transmission of a 4 m long bender relative to a straight channeled guide segment (same coating, same number of channels). For the coating $m = 4.1$ we have $\theta^* = \alpha_c$ for 2 Å neutrons.

the guide entry, is by including the first 9.5 m of the guide system a bender with a radius of curvature 56 m. If the guide width is reduced to 3.5 cm we are out of line-of-sight *once* already at $L^* = 3.96$ m.

The bender must transmit a wavelength band starting at 2 Å, so we require that the bender characteristic angle θ^* is equal to the critical angle of reflection α_c for neutrons with wavelength $\lambda = 2$ Å. For a supermirror with critical scattering vector mQ_{Ni} we have $\alpha_c = \frac{mQ_{\text{Ni}}\lambda}{4\pi}$. From Eq. 1 and Eq. 4 we get

$$w = \frac{R}{2} \left(\frac{mQ_{\text{Ni}}\lambda}{4\pi} \right)^2. \quad (6)$$

Fig. 4A shows Eq. 6 for $\lambda = 2$ Å, $R = 56$ m and $Q_{\text{Ni}} = 0.0217$ Å⁻¹ as function of guide coating m value. Fig. 4B shows the equivalent number of bender channels assuming a total guide width of 5 cm. In Sec. 3.1.2 it is shown that the number of reflections taking place in the bender is proportional to the number of bender channels. Therefore it is of interest to limit the number of bender channels. However, as shown in Fig. 4C the reflectivity decreases with increasing m value. These two competing effects must be accounted for in the final bender design.

3 Neutron guide system and beam transport

3.1 Loss of neutrons in the mirror guide and bender

In this section we estimate the loss of neutrons in the first part of the original guide system consisting of the mirror guide and the bender of total length 4 m. Since the bender design will

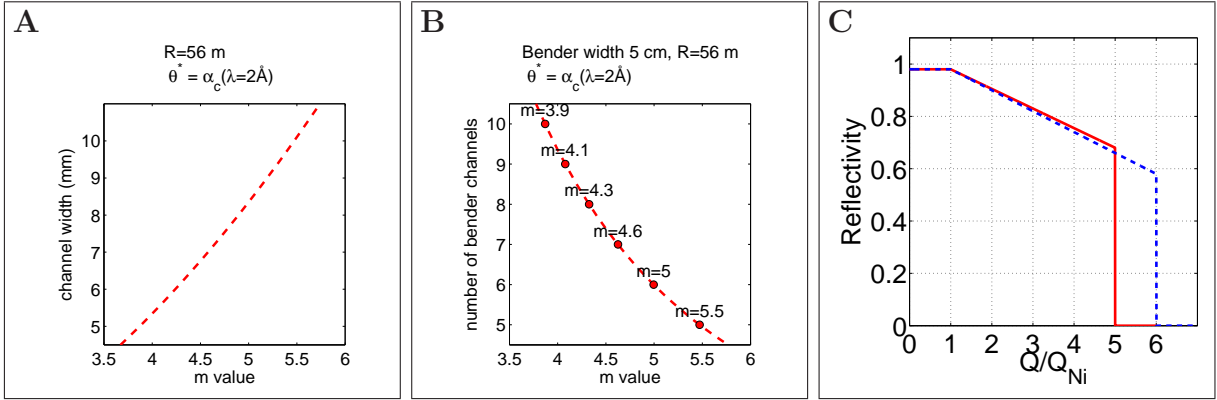


Figure 4: The bender must transmit a wavelength band starting at 2 \AA , so we require that the bender characteristic angle θ^* is equal to the critical angle of reflection α_c for neutrons with wavelength $\lambda = 2\text{ \AA}$.
A: The bender channel width as function of supermirror m value.
B: The number of bender channels as function of supermirror m value for a total guide width of 5 cm.
C: The reflectivity curve of a $m = 5.0$ and a $m = 6$ supermirror. The scattering vector is normalized to the critical scattering vector of Ni, $Q_{\text{Ni}} = 0.0217\text{ \AA}^{-1}$.

be updated to fully account for the line-of-sight elimination, this section can merely be seen as a proof that the simulated results are in agreement with what can be expected from analytical calculations. The transmissions are simulated as function of neutron wavelength, with wavelengthbands 0.001 \AA . If not stated explicitly, the simulated transmissions are compared to the total intensity available at the mirror guide entry. The mirror guide entry is positioned at 2 m from the moderator face and has dimensions 5 cm (w) by 10 cm (h). Horizontally the guide entry is centered at the ESS cold moderator, vertically the guide entry center is 3 cm below the cold moderator center.

The simulations utilize an analytical model for the supermirror reflectivity curve. Fig 4C shows the models for the reflectivity of $m = 5$ and $m = 6$ supermirrors, and the general analytical expression is given in Sec. 2.1.2. We have compared the performance of a mirror/bender unit built of 27 elements with another unit built of 108 elements. The performance is very close to identical, so the simulations are done within the model built of only 27 elements.

3.1.1 Mirror guide transmission

In this section we estimate the transmission of a straight mirror guide of width 5 cm, height 10 cm. The length of the mirror guide is 2.5 m. The losses due to the remaining 1.5 m guide, the bender channels and curvature are treated separately in Sections 3.1.2 and 3.1.3. At the mirror guide entry the total available divergence is limited by distance collimation only. In both horizontal and vertical directions it amounts to about $\pm 2.4^\circ$, which is approximately the double of the critical angle of 2 \AA neutrons (for a $m = 6$ supermirror $\alpha_c = 1.18^\circ$). Therefore we expect the mirror guide to transmit only 25% of the 2 \AA neutrons. For 4 \AA neutrons the critical angle of reflectivity corresponds to the divergence of the beam at the mirror guide entry. Therefore the transmission should be limited by the reflectivity of the supermirrors, see Fig 4C. Fig 5A shows the simulated transmission of a $m = 6$ mirror with side walls made of $m = 5.1$ supermirrors. The simulated results are in agreement with the analytical considerations.

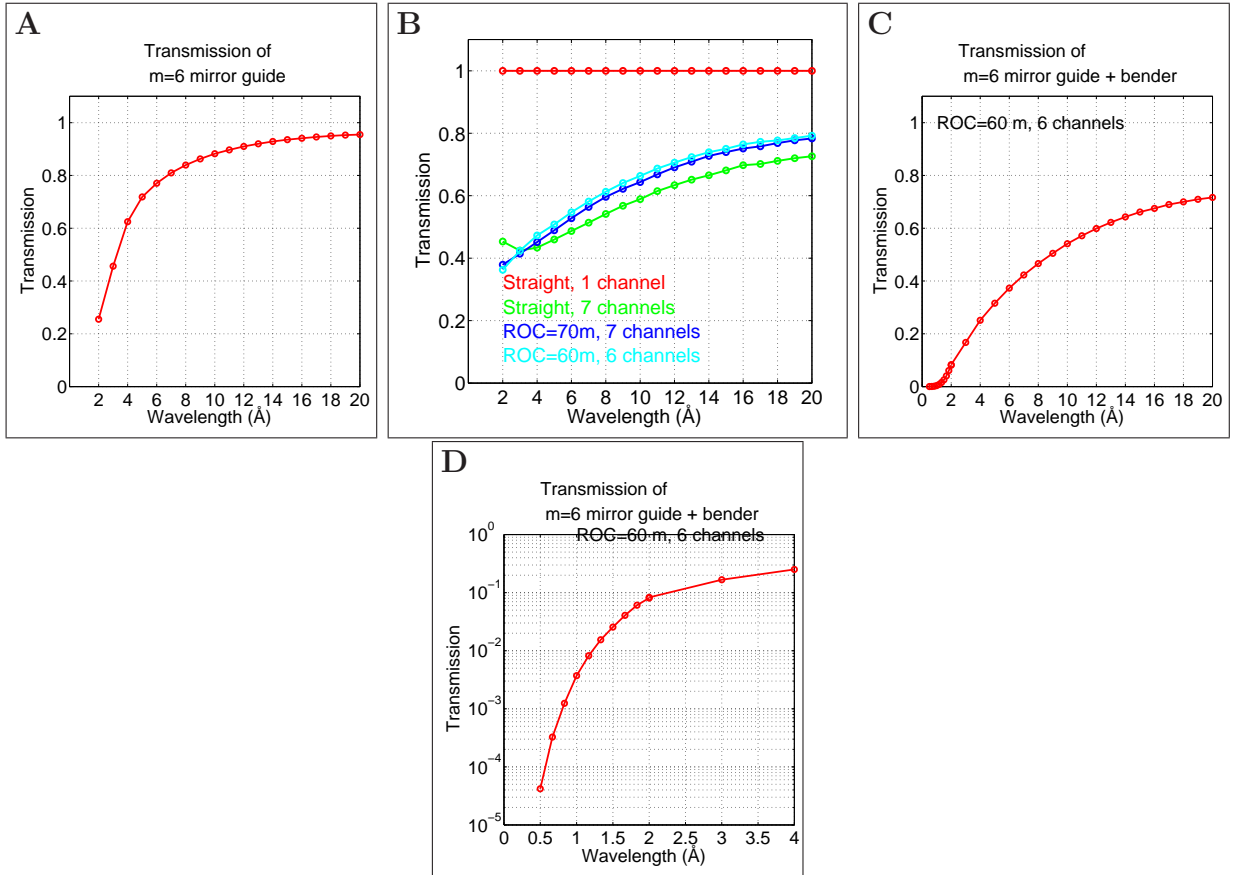


Figure 5: **A**: Simulated transmission of mirror guide. The intensity is normalized to total intensity available at mirror entry
B: Comparison of simulated transmissions of mirror guide, mirror guide with 7 channels and the system mirror guide + bender. Note that here, *the transmission is normalized to the transmission of the straight mirror guide with 1 channel*
C: Simulated transmission of mirror guide + bender. The bender has 6 channels and a radius of curvature of 60 m. The channels are separated by vertical supermirrors with $m_{\text{outer}} = 5.1$, $m_{\text{inner}} = 3.5$. The intensity is normalized to total intensity available at mirror entry
D: The same as **C**, but on a logarithmic scale.

3.1.2 Estimated loss due to bender channels

In this section we consider the loss imposed by the insertion of channels in the straight mirror guide. Further the guide length is increased by 1.5 m to 4 m. The 1.5 m guide has the same width (5 cm) and vertical supermirrors as the mirror guide, but the top and bottom walls are absorbing. In the simulated model the absorbing top and bottom follows the shape of the elliptical guide. The loss due to the curvature of the bender is treated separately in Sec. 3.1.3. Assume that a neutron ray bounces 1 time in a straight guide of length L and width W . This ray may be reflected at a distance between $L/2$ and L from the guide entry, and the angle of reflection θ is in the interval between $2W/L$ and W/L . If the same ray enters a straight guide with N channels, it is reflected after the distance

$$d = \frac{W}{N \tan \theta} \approx \frac{W}{N \theta}, \quad (7)$$

so the number of reflections amounts to

$$N_{\text{reflections}} = \frac{L}{d} = 2N \quad \text{for} \quad \theta = 2W/L, \quad (8)$$

and

$$N_{\text{reflections}} = \frac{L}{d} = N \quad \text{for} \quad \theta = W/L. \quad (9)$$

Fig. 4C shows the reflectivity curve of a $m = 5.0$ supermirror, which is implemented in McStas. To estimate roughly the minimum loss due to the N channels, we assume that the neutrons bounces N times with a reflectivity of 0.9 for the shortest wavelength 2 Å. For a straight guide with 6 channels the transmission then corresponds to 53% compared to a straight guide with one channel. If the guide has 7 channels the transmission is 48%. For the longer wavelengths the supermirror reflectivity is higher (the maximal reflectivity of the supermirror is 0.98) and the transmission scales with R^N . The green curve in Fig. 5B compares the transmission of a straight mirror guide with 7 channels to a straight guide with 1 channel (same total width, same supermirrors). We see that, *relative to the straight guide with 1 channel* the transmission is about 48% for 2 Å neutrons and it increases to about 70% for 20 Å neutrons, corresponding to a reflectivity of 0.95 for 20 Å.

3.1.3 Estimated loss due to bender curvature

We require that the bender characteristic angle is less than or equal to the critical angle of reflection for 2 Å neutrons. Then, for 2 Å neutrons, the transmission of the bender will be at least 67% compared to a straight guide with same number of channels, see also Fig. 3B in Sec. 2.2. The longer wavelengths will have better transmissions. Fig. 5B compares simulated transmissions of 4 m long neutron guides as function of neutron wavelength. Please note that here, *the simulated transmissions are compared to that of a straight guide with 1 channel*. In the simulations, the channels are separated by infinitely thin mirrors, so the loss due to absorption in the channel walls is not included. The figure shows that the simulated transmission of a straight guide with 7 channels amounts to 40%-80%. In accordance with Fig. 3B we see that only at wavelengths shorter than 4 Å the bender transmission is less than the channeled guide transmission. Fig 5C, D show the transmission of the guide system

consisting of the $m = 6$ mirror and the bender (6 channels, radius of curvature 60 m, $m_{\text{outer}} = 5.1$, $m_{\text{inner}} = 3.5$) relative to the total available intensity at the mirror guide entry.

3.1.4 Summary

The transmission of the first 4 m of the guide system is wavelength dependent and ranges from 8% (2 Å) to 72% (20 Å).

The greatest loss of the shortest wavelength (2 Å) is due to the deflection mirror, which transmits only 25% of the available 2 Å neutrons from the cold moderator. The intensity of 2 Å neutrons is further reduced by the presence of the channels: they impose another reduction to about 40%, so we are down to only 10% transmission of the available 2 Å neutrons from the cold moderator. Finally the bender curvature of 60 m reduces the transmission of 2 Å to between 6.7% and 8% depending on the quality of the vertical supermirrors separating the channels.

Based on Sec. 3.1.2 we estimate that the doubling the length of the bender section will reduce the flux of 2 Å neutrons by another factor of 0.48 and the 20 Å neutrons by another factor of 0.7. If it turns out to be sufficient to eliminate line-of-sight only once, the guide width may simply be reduced to 3.5 cm whilst keeping the bender length of 4 m. This will reduce the flux at all neutron wavelengths by a factor of 0.7.

3.2 Loss of neutrons in the elliptical guide

The loss of neutrons in the elliptical guide has not yet been estimated. We envisage to simulate the brilliance transfer to the sample position.

4 Used wavelength range

4.1 Estimated available Q-range

The shorter wavelengths (< 3.3 Å) will illuminate only partly the lower part of the ellipse, so these wavelengths will to some extent be missing in the lower range of grazing angles, that is from 0° to 2.14° . However, considering that the Q -range covered by a given grazing angle θ is

$$Q_{\min} = \frac{4\pi}{\lambda_{\max}} \sin \theta \quad \text{and} \quad Q_{\max} = \frac{4\pi}{\lambda_{\min}} \sin \theta, \quad (10)$$

we see that only the value of Q_{\max} will be affected for grazing angles smaller than 2.14° . To roughly estimate the impact on the reachable Q -range, we can simply assume that the minimum available wavelength at the sample position varies linearly with the grazing angle as shown in Fig. 6A. Assume now that we will cover the Q -range with $Q_{\min} = 0.0033 \text{ }^{-1}$ and $Q_{\max} = 0.45 \text{ }^{-1}$. The red lines of Fig. 6B show how this may be done with the full wavelength range available (2 Å-10 Å) using 5 different grazing angles. If the wavelength range is limited so the minimum wavelength varies with the grazing angle as shown in B, each grazing angle give access to the the Q -ranges indicated by the green lines. So in order to cover the full

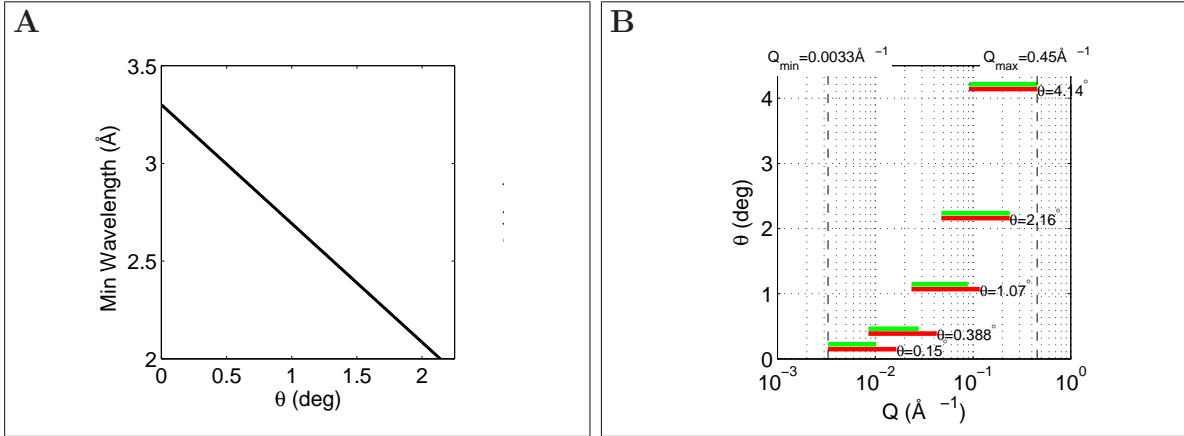


Figure 6: **A**: Assumed available minimum wavelength as function of grazing angle on the sample position. **B**: Q range coverage with the full wavelength range (2 Å-10 Å) is shown with red lines. The green lines indicate the Q ranges covered with the limited wavelength range, that is from the minimum wavelength shown in **A** up to 10 Å.

Q -range *and* have sufficient overlap between the reflectivity curves, it may be necessary to utilize an additional grazing angle, i.e. 6 angles instead of 5.

5 Virtual experiments using standard samples

5.1 Estimation of counting times and realistic errorbars

The simulated intensities I in McStas always have the unit of neutrons/s. Therefore, the counting time for obtaining N_0 counts in a given monitor is then simply estimated as $t = N_0/I$. Counting statistics predicts that for N_0 counts the standard deviation is $\sqrt{N_0}$. Often the simulated errorbars I_{err} are smaller than \sqrt{I} and further the simulated data appears less noisy than real measured data. Therefore, more realistic errorbars are estimated by requiring that the errorbar for N_0 counts is $\sqrt{N_0}$. The missing error $E_{\text{missing}} = \sqrt{N_0 - (t \cdot T_{\text{err}})^2}$ is then added as random noise to the simulated intensities: the noise is random numbers from a normal distribution with mean parameter 0 and standard deviation parameter E_{missing} .

5.2 Conversion of time-of-flight WFM data

The data sets from the virtual experiments using standard samples are simulated as intensity as function of time-of-arrival at the detector position. Fig. 7A shows the direct beam incident on the sample with 4° grazing angle. The 7 WFM pulses are clearly separated in time. To convert the shown time-of-flight data to intensity as function of wavevector transfer Q , we need to know for each wavelength the exact flight time from the mid position between the choppers PSCH1 and PSCH2 to the detector position.

Fig. 7B and C shows how the mean arrival time of each neutron wavelength may be derived from the simulations. These results may also be obtained analytically from the exact chopper geometries, positions, relative phase and frequencies. The neutron take-off times as function of wavelength from the mid position between the choppers PSCH1 and PSCH2 is derived in a

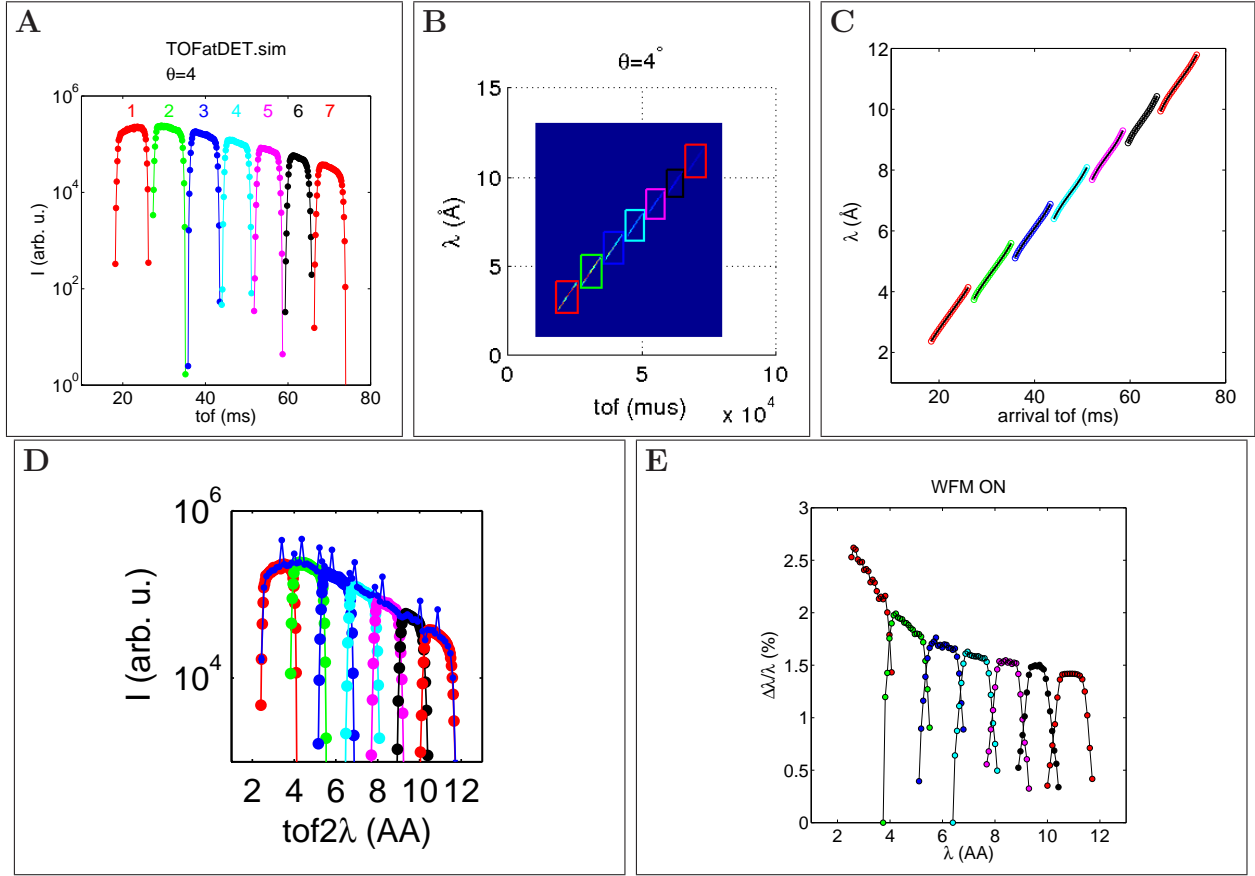


Figure 7: **A**: The positions in time of the 7 different WFM pulses are determined by a time-of-flight sensitive monitor at the detector position. **B**: The information from the high resolution time-of-flight monitor **A** is used to separate the pulses on the wavelength and time-of-flight sensitive monitor at the detector position. **C**: The mean arrival time and time width at the detector for each wavelength is derived from **B**. The circles indicate the mean arrival time as derived from **B**, the black lines is a 3rd order polynomial fitted to the data points. **D**: The simulated intensity as function of the wavelengths calculated from time-of-flight. The big circles with different colors indicate the 7 data sets corresponding to the 7 WFM pulses. The blue points show the same data, but rebinned to a single data set. **E**: The relative wavelength spread as calculated from **B**.

similar way. With the knowledge of the flight path length and the flight time to the detector we can calculate the neutron energy and wavelength from the time-of-flight according to

$$E = 5.22704 \cdot 10^{-6} \left(\frac{L_{\text{flight}}}{t_{\text{flight}}} \right)^2 \quad (11)$$

and

$$\lambda = \frac{2\pi}{\sqrt{E/2.072}}. \quad (12)$$

Fig. 7D shows the intensity as function of wavelengths as calculated from the time-of-flight. We now have the intensity as function of wavelength for the 7 WFM pulses. This data is then rebinned to a single data set and Q is calculated as $4\pi \sin \theta/\lambda$.

5.3 Derivation of Q-resolution from simulated data

The relative wavelength spread $\Delta\lambda/\lambda$ is estimated from the $\Delta t/t_{\text{flight}}$, where Δt is the time spread monitored at the detector position, t_{flight} is the flight time from the mid position time between the choppers PSCH1 and PSCH2 to the detector position and L_{flight} is the flight path length. Fig. 7A and B shows that the WFM pulses may be separated in time. The time-of-flight and wavelength sensitive monitor contains the information about the time spread at the detector for each wavelength bin. The take off time for each wavelength from the mid position time between the choppers PSCH1 and PSCH2 are derived from similar monitors at the relevant position.

6 Optimization using McStas

6.1 The optimization strategy

The aim of the optimization is to obtain an as gap-less as possible distribution of intensity vs grazing angle and horizontal position within an $40 \times 40 \text{ mm}^2$ horizontal area centered in the vicinity of the 2nd focal point of the elliptical guide. In addition to this, the wavelength spectrum reaching the sample should be spatially homogeneous as well as independent of the value of $\Delta\theta/\theta$. The optimization includes 4 independent steps:

1. optimizing the distribution of intensity vs grazing angle at the sample position (at 3\AA)
2. optimizing the beam extraction shielding (ensuring Line Of Sight elimination, reduction of background radiation at the sample position)
3. optimizing the horizontal focusing of the beam
4. optimizing the coating of the guide

Below we outline how the guide was optimised. The remaining optimizations are available on request.

6.2 optimizing the distribution of intensity vs grazing angle at the sample position

The shape of the guide side walls has no impact on the distribution of intensity vs grazing angle at the sample position. Rather it is controlled by the mirror orientation, the guide inclination, the top and bottom guide shape and the relative vertical positions of the moderator, the mirror, the guide and the sample. In order to improve statistics for this part of the optimization, only neutrons with zero horizontal divergence have been included in the simulations.

The wavelength spectrum of interest is spans from 2\AA to 10\AA . However, during this part of the optimization, the wavelength band is limited to 0.001\AA centered at 3\AA . This is to ensure

that the optimized guide will transport both short and longer wavelengths, since the longer wavelengths have a larger critical angle of reflection. The coating of mirror is $m=6$. For the optimizations, the guide coating is $m=6$. This is solely to avoid the situation where the guide shape is controlled by some arbitrary choice of m -value distribution through the guide. The optimal distribution of m -values (which is far from $m=6$ all the way), taking also cost into account, is determined after the guide shape is fixed. The Figure-Of-Merit used in the optimization is the intensity monitored within a $40 \times 40\text{mm}^2$ horizontal area centered at the sample position. The FOM-monitor includes only the neutrons with grazing angles in the interval $0^\circ-4^\circ$.

Table 1 shows the parameter values varied in the the optimization.

PARAMETER	DESCRIPTION
Y_sample	Vertical position of the sample
Y_mirror	Vertical position of the deflection mirror
Y_guide	Vertical position of the guide
focus_inh	1st focal point position
focus_outh	2nd focal point position
smallaxis_w	Ellipse minor axis
T_mirror	Mirror inclination
TT_guide	Guide inclination

Table 1: Parameters for the optimization including the mirror and the top/bottom shape of the guide.

7 Comparison of McStas 1.12c and McStas 2.0 simulated results

The work presented is based entirely on simulated data originating from the neutron ray-trace simulation package McStas². The simulation work is conducted using two different versions of McStas, namely version 1.12c and 2.0. The versions have different models of the ESS cold source, both regarding geometry and flux as function of wavelength. For this concept the change of moderator geometry has had no noteworthy impact on the results. However, when comparing the flux from instruments simulated within different versions 1.12c and 2.0 of McStas, the results must be scaled according to Fig. 8A.

When comparing the simulated results from the 2 different McStas versions, ideally we should compare identical instruments simulated in version 1.12c and 2.0. However, due to limited resources we have not done that yet. In this section we compare the flux at the sample position as simulated with two different realizations of the FREIA instrument, one is simulated within 1.12c and the other within 2.0. The purpose of the comparison is to point out general differences and common features in the range of grazing angles available. The observed differences are well understood from the different instrument layouts.

7.1 Differences in instrument layout and consequences for the flux distribution

For both instruments the sample to detector distance is 3 m and a moderator to sample distance of 27 m. The guide ends 2 m from the sample position, leaving space for a pair of

²mcstas.org

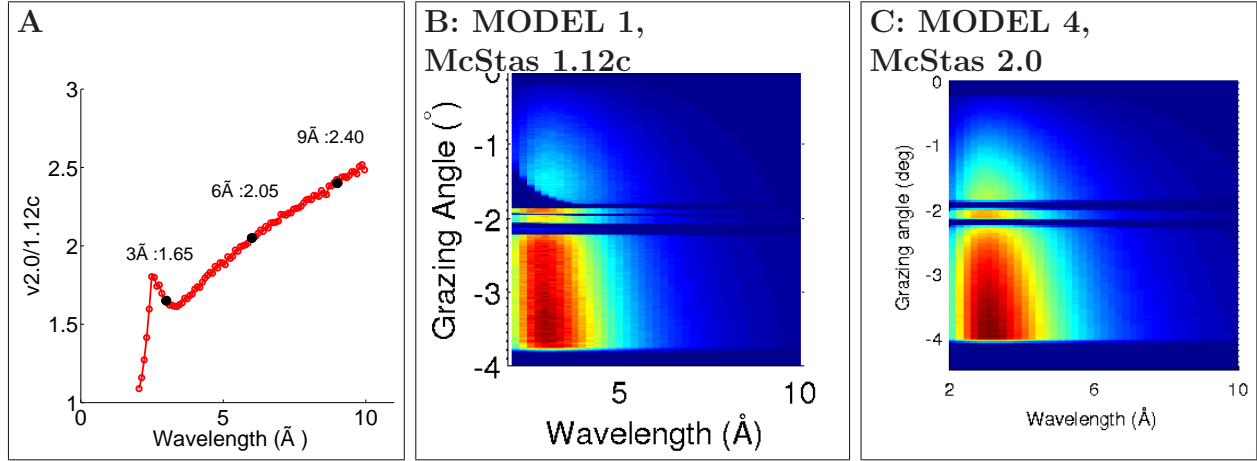


Figure 8: **A:** Comparing the flux of the cold source in McStas 2.0 with that of McStas 1.12c. **B, C:** The shown data is output from a horizontal wavelength and grazing angle sensitive $4 \times 4 \text{ cm}^2$ monitor at the sample position. The angle defining slits 1 and 2 are wide open. **B:** The flux distribution at the horizontal sample position as simulated with the cold source in McStas 1.12c and instrument MODEL 1. **C:** The flux distribution at the horizontal sample position as simulated with the cold source in McStas 2.0 and instrument MODEL 4.

grazing angle defining slits. The slits are separated by 1.5 m, leaving a space of 0.5 m from the last slit to the sample. The differences between the two models are outlined below:

MODEL 1: The neutrons are reflected by a 2.5 m long mirror rotated around the x axis (horizontal, perpendicular to upstream-downstream direction) positioned 3.25 m from the moderator surface. The mirror is followed by an elliptical guide, rotated about 2° around the x axis 3.25 m from the moderator surface. The guide has a rectangular cross section, with the shape of top/bottom and side walls defined by 2 different ellipses.

MODEL 4: An elliptical guide extends from 2 m from the moderator surface to 25 m. The guide has a rectangular cross section, with the shape of top/bottom being elliptic and the side walls are straight. The guide width is 40 mm and is curved to a radius of curvature of 350 m in the (nearly horizontal) plane spanned by the guide major axis and the x axis.

MODEL 1 is similar to the proposed instrument since it do have the neutrons reflected into the guide by a deflection mirror. In Sec. 1 is described how the deflection mirror strongly affects the sample flux at low grazing angle of the 2 \AA - 3 \AA neutrons. Fig. 8B and C shows clearly that a removal of the mirror improves the transport of 2 \AA - 3 \AA neutrons to low grazing angles at the sample.

7.2 Sample flux comparison

The purpose of this section is to document that the two different version of McStas give comparable flux numbers at the sample. Table 2 compares the performance of models 1, 4 in terms of the flux at the sample position averaged over a $4 \times 4 \text{ cm}^2$ horizontal area centered at the sample position. Models 4 is simulated using McStas 2.0, whereas Model 1 is simulated using McStas 1.12c. For the comparison, the flux numbers of Model 1 are scaled according to Fig. 8A, which compares the cold source intensity of version 2.0 with that of version 1.12c. To ease the comparison, the flux numbers of Model 4 are also given as percentages of the corresponding Model 1 flux numbers. As expected the flux is dramatically decreased by

Time averaged flux numbers $\Delta\theta/\theta = 3\%$							
	Angle θ	Flux (n/s/cm ² /Å) at wavelength					
		3 Å		6 Å		9 Å	
Mirror+elliptical guide(h,v) (MODEL 1)	0.5°	(1.9e5)	3.2e5	(5.3e4)	1.1e5	(1.1e4)	2.6e4
	1.5°	(2.3e6)	3.7e6	(5.1e5)	1.1e6	(9.7e4)	2.3e5
	3.5°	(1.3e7)	2.1e7	(2.9e6)	6.0e6	(5.4e5)	1.3e6
No Mirror+ROC 350m +elliptical guide(h) (MODEL 4)	0.5°	1.5e5 (47%)		4.8e4 (44%)		1.3e4 (49%)	
	1.5°	1.4e6 (38%)		4.2e5 (41%)		1.2e5 (50%)	
	3.5°	6.9e6 (33%)		2.3e6 (39%)		6.3e5 (49%)	

Table 2: Comparison of time averaged flux at wavelengths 3 Å, 6 Å and 9 Å for grazing angles 0.5°, 1.5°, 3.5°. For MODEL 1, the flux numbers in the grey boxes are obtained with McStas version 1.12c. To compare MODEL 1 to MODEL 4, the flux numbers are scaled according Fig. 8A, which compares the cold source intensity of version 2.0 with that of version 1.12c.

replacing the elliptical guide side walls (MODEL 1) with straight guide walls.

Fig 8 compares Models 1 and 4 in terms of the output from a horizontal wavelength and grazing angle sensitive 4×4 cm² monitor at the sample position. Model 1 is simulated with McStas 1.12c whereas Model 4 is simulated with McStas 2.0. The surface plots show that the range of grazing angles obtainable are similar, from 0.25° to 4.1°. Both models have gaps in the intensity around 2°, caused by a combination of the incompleteness of the elliptical guide shape and limitations in the divergence range available at the guide entry. For Model 4 the gaps are of similar angular width for all wavelengths. For Model 1 the lowest wavelengths 2–3 Å have noteworthy wider angular gaps than the remaining part of the wavelength range. This detail is caused by the limitations of the deflecting mirror reflectivity for the lowest wavelengths.

7.3 Summary

In general there is a good agreement between the simulated results obtained with McStas 2.0 and McStas 1.12c. The differences observed here is merely due to differences in instrument layout. Most important there is no unexpected increase in the flux at the sample position.